Exclusive π^0 electroproduction at $W > 2$ GeV with CLAS

I. Bedlinskiy,[19] V. Kubarovsky,[32,27] S. Niccolai,[18,12] P. Stoler,[27] K. P. Adhikari,[26] M. D. Anderson,[35] S. Anefalos Pereira,[15] H. Avakian,[32] J. Ball,[6] N. A. Baltzell,[1,31] M. Battaglieri,[16] V. Batourine,[32,21] A. S. Biselli,[9] S. Boiarinov,[32] J. Bono,[10] W. J. Briscoe,[12] W. K. Brooks,[33,32] V. D. Burkert,[32] D. S. Carman,[32] A. Celentano,[16] S. Chandavar,[25] L. Colaneri,[17] P. L. Cole,[13] M. Contalbrigo,[14] O. Cortes,[13] V. Crede,[11] A. D'Angelo,[17,29] N. Dashyan,[39] R. De Vita,[16] E. De Sanctis,[15] A. Deur,[32] C. Djalali,[31] D. Doughty,[7,32] R. Dupre,[18] H. Egiyan,[32,23] A. El Alaoui,[1,*] L. El Fassi,[26] L. Elouadrhiri,[32] P. Eugenio,[11] G. Fedotov,[31,30] S. Fegan,[16] J. A. Fleming,[34] T. A. Forest,[13] B. Garillon,[18] M. Garçon,[6] G. Gavalian,[26] N. Gevorgyan,[39] Y. Ghandilyan,[39] G. P. Gilfoyle,[28] K. L. Giovanetti,[20] F. X. Girod,[32,6] E. Golovatch,[30] R. W. Gothe,[31] K. A. Griffioen,[38] B. Guegan,[18] M. Guidal,[18] L. Guo,[10,32] K. Hafidi,[1] H. Hakobyan,[33,39] N. Harrison,[8] M. Hattawy,[18] K. Hicks,[25] M. Holtrop,[23] D. G. Ireland,[35] B. S. Ishkhanov,[30] E. L. Isupov,[30] D. Jenkins,[36] H. S. Jo,[18] K. Joo,[8] D. Keller,[37] M. Khandaker,[13,24] A. Kim,[8] W. Kim,[21] A. Klein,[26] F. J. Klein,[5] S. Koirala,[26] S. E. Kuhn,[26] S. V. Kuleshov,[33,19] P. Lenisa,[14] W. I. Levine,[4] K. Livingston,[35] H. Y. Lu,[31] I. J. D. MacGregor,[35] N. Markov,[8] M. Mayer,[26] B. McKinnon,[35] M. Mirazita,[15] V. Mokeev,[32,30] R. A. Montgomery,[15,†] C. I. Moody,[1] H. Moutarde,[6] A. Movsisyan,[14] C. Munoz Camacho,[18] P. Nadel-Turonski,[32,12] I. Niculescu,[20] M. Osipenko,[16] A. I. Ostrovidov,[11] L. L. Pappalardo,[14] K. Park,[32,21] S. Park,[11] E. Pasyuk,[32] E. Phelps,[31] W. Phelps,[10] J. J. Phillips,[35] S. Pisano,[15] O. Pogorelko,[19] J. W. Price,[3] Y. Prok,[26,32,37] D. Protopopescu,[35] S. Procureur,[6] A. J. R. Puckett,[8] B. A. Raue,[10,32] M. Ripani,[16] B. G. Ritchie,[2] A. Rizzo,[17,‡] P. Rossi,[15,32] P. Roy,[11] F. Sabatié,[6] C. Salgado,[24] D. Schott,[12] R. A. Schumacher,[4] E. Seder,[8] I. Senderovich,[2] Y. G. Sharabian,[32] A. Simonyan,[39] G. D. Smith,[34,†] D. I. Sober,[5] D. Sokhan,[35,18] S. S. Stepanyan,[21] S. Strauch,[31,12] V. Sytnik,[33] W. Tang,[25] Ye Tian,[31] M. Ungaro,[32,8] A. V. Vlassov,[19] H. Voskanyan,[39] E. Voutier,[22] N. K. Walford,[5] D. Watts,[35] X. Wei,[32] L. B. Weinstein,[26] M. Yurov,[37] N. Zachariou,[31] L. Zana,[34,23] J. Zhang,[32,26] Z. W. Zhao,[37,31] and I. Zonta[17,‡]

(CLAS Collaboration)

[1]*Argonne National Laboratory, Argonne, Illinois 60439, USA*
[2]*Arizona State University, Tempe, Arizona 85287-1504, USA*
[3]*California State University, Dominguez Hills, Carson, California 90747, USA*
[4]*Carnegie Mellon University, Pittsburgh, Pennsylvania 15213, USA*
[5]*Catholic University of America, Washington, DC 20064, USA*
[6]*CEA, Centre de Saclay, Irfu/Service de Physique Nucléaire, 91191 Gif-sur-Yvette, France*
[7]*Christopher Newport University, Newport News, Virginia 23606, USA*
[8]*University of Connecticut, Storrs, Connecticut 06269, USA*
[9]*Fairfield University, Fairfield Connecticut 06824, USA*
[10]*Florida International University, Miami, Florida 33199, USA*
[11]*Florida State University, Tallahassee, Florida 32306, USA*
[12]*The George Washington University, Washington, DC 20052, USA*
[13]*Idaho State University, Pocatello, Idaho 83209, USA*
[14]*INFN, Sezione di Ferrara, 44100 Ferrara, Italy*
[15]*INFN, Laboratori Nazionali di Frascati, 00044 Frascati, Italy*
[16]*INFN, Sezione di Genova, 16146 Genova, Italy*
[17]*INFN, Sezione di Roma Tor Vergata, 00133 Rome, Italy*
[18]*Institut de Physique Nucléaire ORSAY, Orsay, France*
[19]*Institute of Theoretical and Experimental Physics, Moscow 117218, Russia*
[20]*James Madison University, Harrisonburg, Virginia 22807, USA*
[21]*Kyungpook National University, Daegu 702-701, Republic of Korea*
[22]*LPSC, Universite Joseph Fourier, CNRS/IN2P3, INPG, Grenoble, France*
[23]*University of New Hampshire, Durham, New Hampshire 03824-3568, USA*
[24]*Norfolk State University, Norfolk, Virginia 23504, USA*
[25]*Ohio University, Athens, Ohio 45701, USA*
[26]*Old Dominion University, Norfolk, Virginia 23529, USA*
[27]*Rensselaer Polytechnic Institute, Troy, New York 12180-3590, USA*
[28]*University of Richmond, Richmond, Virginia 23173, USA*
[29]*Universita' di Roma Tor Vergata, 00133 Rome, Italy*
[30]*Skobeltsyn Institute of Nuclear Physics, Lomonosov Moscow State University, 119234 Moscow, Russia*
[31]*University of South Carolina, Columbia, South Carolina 29208, USA*
[32]*Thomas Jefferson National Accelerator Facility, Newport News, Virginia 23606, USA*
[33]*Universidad Técnica Federico Santa María, Casilla 110-V Valparaíso, Chile*
[34]*Edinburgh University, Edinburgh EH9 3JZ, United Kingdom*
[35]*University of Glasgow, Glasgow G12 8QQ, United Kingdom*
[36]*Virginia Polytechnic Institute and State University, Blacksburg, Virginia 24061-0435, USA*

[37] *University of Virginia, Charlottesville, Virginia 22901, USA*
[38] *College of William and Mary, Williamsburg, Virginia 23187-8795, USA*
[39] *Yerevan Physics Institute, 375036 Yerevan, Armenia*
(Received 1 May 2014; published 13 August 2014; corrected 29 August 2014)

Exclusive neutral-pion electroproduction ($ep \to e'p'\pi^0$) was measured at Jefferson Lab with a 5.75-GeV electron beam and the CLAS detector. Differential cross sections $d^4\sigma/dtdQ^2dx_Bd\phi_\pi$ and structure functions $\sigma_T + \epsilon\sigma_L$, σ_{TT}, and σ_{LT} as functions of t were obtained over a wide range of Q^2 and x_B. The data are compared with Regge and handbag theoretical calculations. Analyses in both frameworks find that a large dominance of transverse processes is necessary to explain the experimental results. For the Regge analysis it is found that the inclusion of vector meson rescattering processes is necessary to bring the magnitude of the calculated and measured structure functions into rough agreement. In the handbag framework, there are two independent calculations, both of which appear to roughly explain the magnitude of the structure functions in terms of transversity generalized parton distributions.

DOI: 10.1103/PhysRevC.90.025205 PACS number(s): 13.60.Le, 14.20.Dh, 14.40.Be, 24.85.+p

I. INTRODUCTION

Understanding nucleon structure in terms of the fundamental degrees of freedom of quantum chromodynamics is one of the main goals in the theory of strong interactions. The nucleon is a many-body system of quarks and gluons. How partons move and how they are distributed in space is still an open question on which new theoretical and experimental developments are starting to shed a new light. The study of deep inelastic scattering provides the distribution of longitudinal momentum and polarization carried by quarks and antiquarks within the fast moving hadron. However, the spatial distribution of the partons in the plane perpendicular to the hadron motion is not accessible in these experiments. The role of the partons' orbital angular momenta in making up the total spin of the nucleon is one more unresolved question. In recent years it became clear that exclusive reactions may provide such information encoded in so-called generalized parton distributions (GPDs) [1,2]. The GPDs describe the simultaneous distribution of partons with respect to both the partons' transverse positions and longitudinal momenta. In addition to the information about transverse spatial density (form factors) and momentum density, these functions reveal the correlation of the spatial and momentum distributions, i.e., how the spatial shape of the nucleon changes when probing quarks of different longitudinal momenta. GPDs give access as well to the total angular momentum carried by partons, comprising the spin and orbital parts [1].

The possibility to study GPDs in exclusive scattering processes rests on factorization theorems, which are proven for virtual Compton scattering [3] and light meson electroproduction [4] in the limit of $Q^2 \to \infty$, at fixed x_B and t. Here $q^2 \equiv -Q^2$ is the square of the 4-momentum transferred to the hadronic system by the scattered electron, $-t$ is the 4-momentum transferred to the recoiling proton, and x_B is the Bjorken variable. These proofs are based on the properties of matrix elements represented by Feynman diagrams colloquially referred to as handbags [1,2,5]. The reaction is factorized into two parts. One part treats the elementary interaction with one of the partons in the nucleon perturbatively, while the nonperturbative remainder is embodied in GPDs. While the perturbative process between the virtual photon and the quark is reaction dependent, the information contained within the GPDs is universal. Figure 1 indicates the lowest-order handbag mechanism applied to three reactions: elastic scattering, deeply virtual Compton scattering (DVCS), and deeply virtual meson electroproduction (DVMP), which is the subject of this article.

While the handbag mechanism should be mostly applicable at asymptotically large photon virtuality Q^2, there is some experimental evidence [6] that the DVCS reaction at Q^2 as low as 1.5 GeV^2 appears to be applicable by the handbag mechanism. This is not unexpected because both vertices of the Compton scattering reaction from a single quark involve perturbative electromagnetic processes. However, for DVMP, the second vertex [πqq in Fig. 1(c)] involves the exchange of at least one gluon, and the kinematic range of leading-order applicability of the handbag formalism is not as clearly determined.

There are eight GPDs. Four correspond to parton helicity-conserving (chiral-even) processes, denoted by H^q, $\tilde{H}^q$, E^q, and $\tilde{E}^q$, and four correspond to parton helicity-flip (chiral-odd) processes [7,8], H_T^q, $\tilde{H}_T^q$, E_T^q, and $\tilde{E}_T^q$. At a given Q^2 the GPDs depend on three kinematic variables: x, ξ, and t. In a symmetric frame, x is the average longitudinal momentum fraction of the struck parton before and after the hard interaction and ξ (skewness) is half of the longitudinal momentum fraction transferred to the struck parton. The skewness can be expressed in terms of the Bjorken variable x_B as $\xi \simeq x_B/(2 - x_B)$. Here $x_B = Q^2/(2pq)$ and $t = (p - p')^2$, where p and p' are the initial and final 4-momenta of the nucleon. The GPDs encode both the longitudinal momentum distributions through their dependence on x and the transverse position distributions through their dependence on t.

In the forward limit where $t \to 0$, H^q, and $\tilde{H}^q$ reduce to the parton density distributions $q(x)$ and parton helicity

*Current address: Universidad Técnica Federico Santa María, Casilla 110-V Valparaíso, Chile.
†Current address: University of Glasgow, Glasgow G12 8QQ, United Kingdom.
‡Current address: Universita' di Roma Tor Vergata, 00133 Rome, Italy.

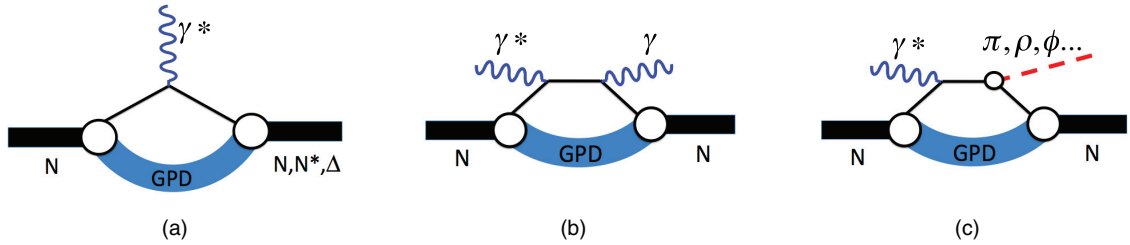

FIG. 1. (Color online) Schematic diagram of the lowest-order handbag mechanism applied to: (a) elastic scattering, (b) DVCS, and (c) meson production.

distributions $\Delta q(x)$, respectively. The first moments in x of the chiral-even GPDs are related to the elastic form factors of the nucleon: the Dirac form factor $F_1^q(t)$, the Pauli form factor $F_2^q(t)$, the axial-vector form factor $g_A^q(t)$, and the pseudoscalar form factor $h_A^q(t)$ [9].

The DVMP process specifically for π^0 production is shown in more detail in Fig. 2.

It was shown early on [10] that for pion electroproduction the leading handbag approach is valid at large Q^2 for longitudinal helicity-conserving virtual photons. Using Regge phenomenology as a guide for parametrization of the four longitudinal GPDs, Refs. [11,12] calculated cross-section structure functions for longitudinal helicity-conserving virtual photons. Simultaneously, the CLAS Collaboration, as well as other groups [13–15], measured the differential cross sections for pion electroproduction and extracted structure functions, which are the subject of the present paper.

When the theoretical calculations for longitudinal virtual photons were compared with the JLab data, as well as with HERMES data, they were found to underestimate the measured cross sections by more than an order of magnitude in their accessible kinematic regions, even after including finite-size corrections through Sudakov form factors [12]. At JLab, sizable beam-spin asymmetries for exclusive neutral-pion electroproduction off the proton were measured [16] above the resonance region. These nonzero asymmetries imply that

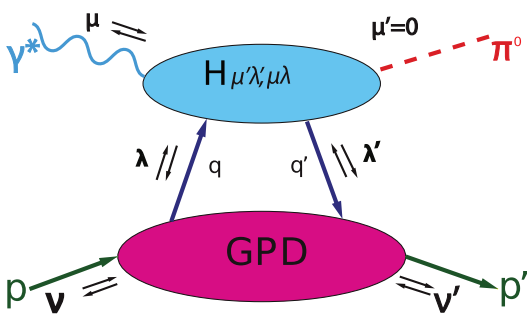

FIG. 2. (Color online) Schematic diagram of the π^0 electroproduction amplitude in the framework of the handbag mechanism. The helicities of the initial and final nucleons are denoted by ν and ν', of the incident photon and produced meson by μ and μ', and of the active initial and final quark by λ and λ'. The arrows in the figure schematically represent the corresponding positive and negative helicities, respectively. For final-state photons or vector mesons $\mu' = \pm 1$, while for pseudoscalar mesons $\mu' = 0$.

both transverse and longitudinal amplitudes participate in the process.

The failure to describe the experimental results with quark helicity-conserving operators [9,11] stimulated a consideration of the role of the chiral-odd quark helicity-flip processes. Pseudoscalar meson electroproduction, and in particular π^0 production in the reaction $ep \to e'p'\pi^0$, was identified [12,17,18] as especially sensitive to the quark helicity-flip subprocesses. The produced meson has no intrinsic helicity so that the angular momentum of the incident photon is either transferred to the nucleon via a quark helicity-flip or involves orbital angular momentum processes. Evidence of the contribution of helicity-flip subprocesses, especially H_T, to π^+ electroproduction in transverse target spin asymmetry data [15] was noted in Ref. [12]. A disadvantage of π^+ production is that the interpretation is complicated by the dominance of the longitudinal π^+-pole term, which is absent in π^0 production. In addition, for π^0 production the structure of the amplitudes further suppresses the quark helicity-conserving amplitudes relative to the helicity-flip amplitudes [12]. However, π^0 cross sections over a large kinematic range are much more difficult to obtain than for π^+ because the clean detection of π^0's requires the measurement of their two decay photons.

During the past few years, two parallel theoretical approaches—(GL) [17,19] and (GK) [12,18]—have been developed utilizing the chiral-odd GPDs in the calculation of pseudoscalar meson electroproduction. The GL and GK approaches, though employing different models of GPDs, lead to *transverse* photon amplitudes that are much larger than the longitudinal amplitudes.

At the same time the most successful theoretical approaches for describing exclusive reactions in the past have been those based upon the Regge model, which was introduced in the 1960s. The Regge model [20] has continued to provide insights into the nature of hadrons and their interactions.

The comparison of the results of GL and GK with each other and with the results obtained by the analysis of some of the CLAS data was discussed in Ref. [13].

This paper presents the complete results of that experiment and a comprehensive description of the data analysis, following the description of the experiment. The experimental results will be compared with those of GL and GK, as well as with the most advanced Regge model predictions [20] for the π^0 exclusive production over a wider range of kinematic intervals than previously available.

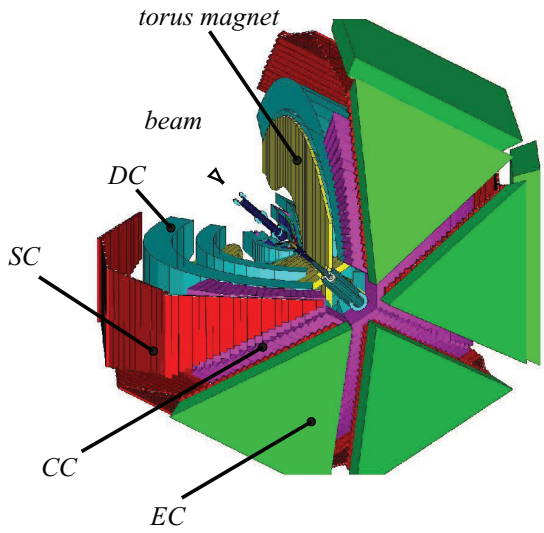

FIG. 3. (Color online) Three-dimensional schematic view of the elements of the CLAS detector with the different subsystems labeled. A single sector of the detector has been cut away to enable a view of the inner subsystems. The diameter of the CLAS detector was ∼10 m. The notation is as follows: EC, electromagnetic calorimeter; CC, Cherenkov counter; SC, scintillation hodoscope; DC, drift chambers.

The main goal of the experiment was to measure the differential cross section $\frac{d^4\sigma}{dQ^2 dx_B dt d\phi_\pi}$ of the reaction $ep \to e'p'\pi^0$ in bins of Q^2, x_B, t, and ϕ_π, where ϕ_π is the angle of the final-state hadronic plane relative to the electron scattering plane. Fits to the ϕ_π dependence [see Appendix B, Eq. (B1)], in each bin of Q^2, x_B and t, give access to the structure functions $(\sigma_T + \epsilon\sigma_L)$, σ_{TT}, and σ_{LT}.

II. EXPERIMENTAL SETUP

The measurements reported here were carried out with the CEBAF Large Acceptance Spectrometer (CLAS) [21] located in Hall B at Jefferson Lab. A three-dimensional view of CLAS with the different subsystems labeled is shown in Fig. 3. The data were taken with a 5.75-GeV electron beam and a 2.5-cm-long liquid-hydrogen target. The target was placed 66 cm upstream of the nominal center of CLAS inside a solenoid magnet to shield the detectors from Møller electrons. The spectrometer was operated at an instantaneous luminosity of 2×10^{34} cm^{-2} s^{-1}. The scheme of the CLAS geometry, as coded in the GEANT3-based CLAS simulation code GSIM, is shown in Fig. 4. CLAS consisted of six identical sectors with an approximately toroidal magnetic field. Each sector was equipped with three regions of drift chambers (DCs) [22]

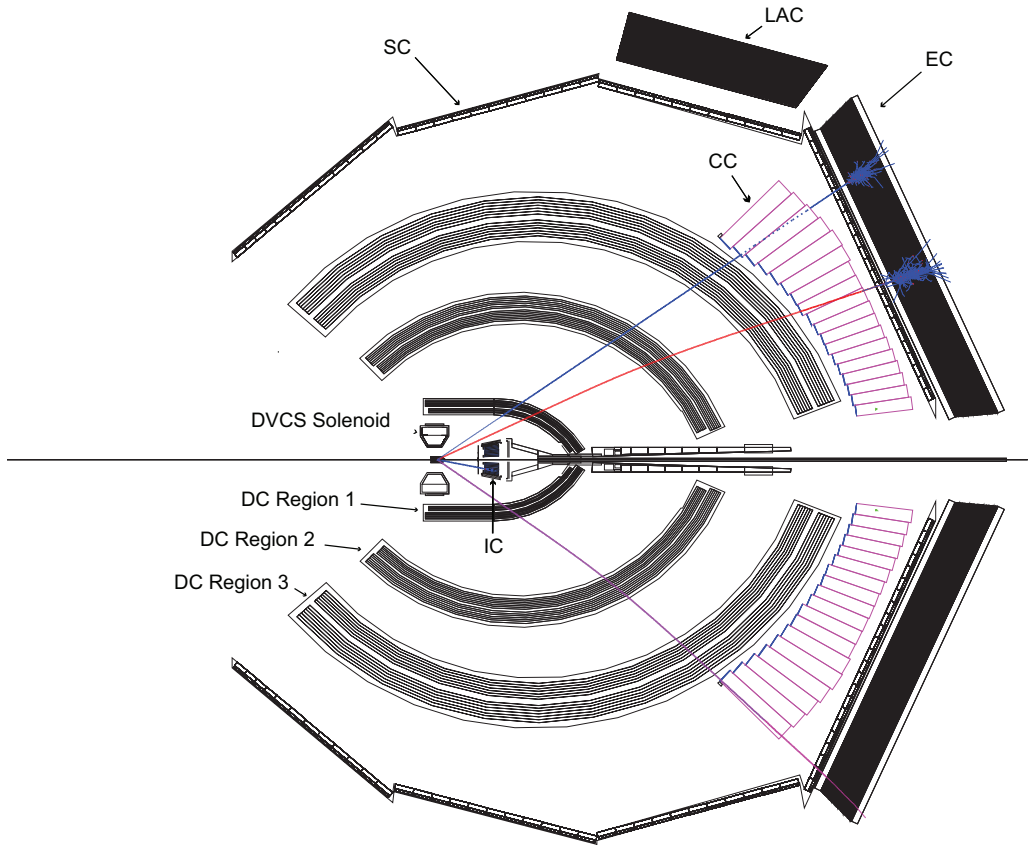

FIG. 4. (Color online) Schematic view of the CLAS detector constructed by the Monte Carlo simulation program GSIM. Note: IC, inner calorimeter; EC, electromagnetic calorimeter; LAC, large-angle electromagnetic calorimeter; CC, Cherenkov counter; SC, scintillation hodoscope; DC, drift chambers. The LAC was not used in this analysis. The tracks correspond, from top to bottom, to a photon (blue), an electron (red) curving toward the beam line, and a proton (purple) curving away from the beamline.

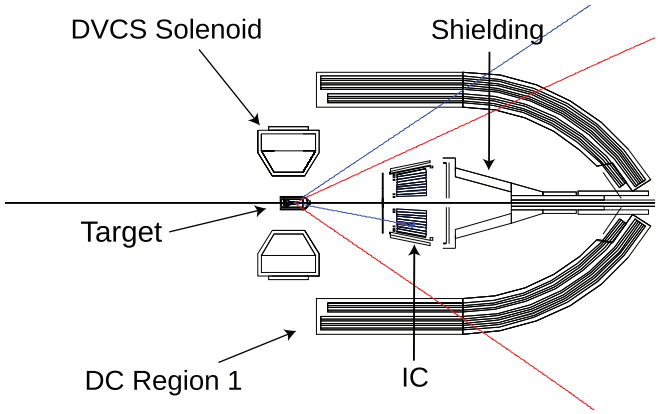

FIG. 5. (Color online) A magnification of Fig. 4 showing the CLAS target region in detail. IC is the inner calorimeter and DC region 1 represents the DCs closest to the target.

to determine the trajectory of charged particles, gas threshold Cherenkov counters (CCs) [23] for electron identification, a scintillation hodoscope [24] for time-of-flight (TOF) measurement of charged particles, and an electromagnetic calorimeter (EC) [25] which was used for electron identification as well as detection of neutral particles. To detect photons at small polar angles (from 4.5° up to 17°) an inner calorimeter (IC) was added to the standard CLAS configuration, 55 cm downstream from the target. Figure 5 zooms in on the target area of Fig. 4 to better illustrate the deployment of the IC and solenoid relative to the target. The IC consisted of 424 $PbWO_4$ tapered crystals whose orientations were projected somewhat upstream of the target. Each crystal had a 13.3×13.3 mm^2 square front face, a 16×16 mm^2 rear face, and 160 mm of length. The light from each crystal was collected with an avalanche photodiode followed by a low-noise preamplifier. The temperature of the IC was stabilized with $<0.1^\circ$ C precision. The toroidal magnet was operated at a current corresponding to a magnetic field integral of about 1.36 T-m in the forward direction. The magnet polarity was set such that negatively charged particles were bent inward towards the electron beamline. The scattered electrons were detected in the CC and EC, which extended from 21° to 45°. The lower limit was defined by the IC calorimeter located just after the target. A totally absorbing Faraday cup was used to determine the integrated beam charge passing through the target.

In the experiment, all four final-state particles of the reaction $ep \to e'p'\pi^0$, $\pi^0 \to \gamma\gamma$ were detected. The kinematic coverage for this reaction is shown in Fig. 6, and that for the individual kinematic variables is shown in Fig. 7. For the purpose of physics analysis, an additional cut on $W > 2$ GeV was applied as well, where W is the $\gamma^* p$ center-of-mass energy.

The basic configuration of the trigger included the coincidence between signals from two detectors in the same sector: the CC and the EC with a threshold ~500 MeV. Of a total of about 7×10^9 recorded events, about 1×10^5 events for the reaction of interest were finally retained. The specific experimental data set ("e1-dvcs") used for this analysis was collected in 2005. The integrated luminosity collected was

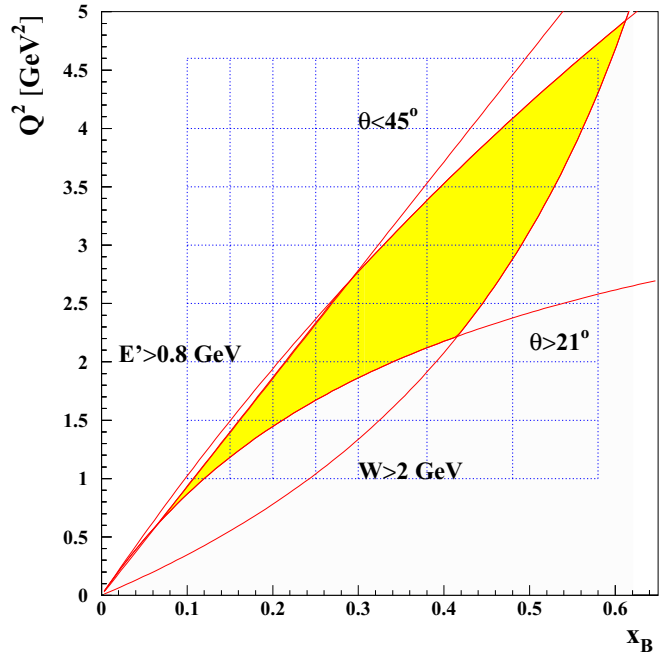

FIG. 6. (Color online) The kinematic coverage and binning as a function of Q^2 and x_B. The accepted region (yellow online) is determined by the following cuts: $W > 2$ GeV, $E' > 0.8$ GeV, $21^\circ < \theta < 45^\circ$. W is the $\gamma^* p$ center-of-mass energy, E' is the scattered electron energy, and θ is the electron's polar angle in the laboratory frame. The dotted grid represents the kinematic regions for which the cross sections are calculated and presented.

31.4 fb^{-1}. However, not all data were used for the measurement of the cross section. After applying strict run-to-run stability criteria, the integrated luminosity corresponding to the data presented here was 19.9 fb^{-1}.

III. PARTICLE IDENTIFICATION

A. Electron identification

An electron was identified by requiring the track of a negatively charged particle in the DCs to be matched in time and space with hits in the CC, the EC, and the SC in the same sector of CLAS. This electron selection effectively suppresses π^- contamination up to momenta ~2.5 GeV. Additional requirements were used in the offline analysis to refine electron identification and to suppress the remaining pions. Geometric "fiducial" cuts were applied in such a way that only regions in the CC and EC that had high electron efficiency were used.

Energy deposition cuts on the electron signal in the EC also play an important role in suppressing background. An electron propagating through the calorimeter produces an electromagnetic shower and deposits a large fraction of its energy in the calorimeter proportional to its momentum, while pions typically lose a smaller fraction of their energy primarily by ionization. For an electron, the observed energy-to-momentum ratio $E_{\rm cal}/p$ is known as the sampling fraction. The observed sampling fraction vs momentum is shown in Fig. 8. The electron events are broadly clustered near $E_{\rm cal}/p \sim 0.25$. A cut was then applied to select events within

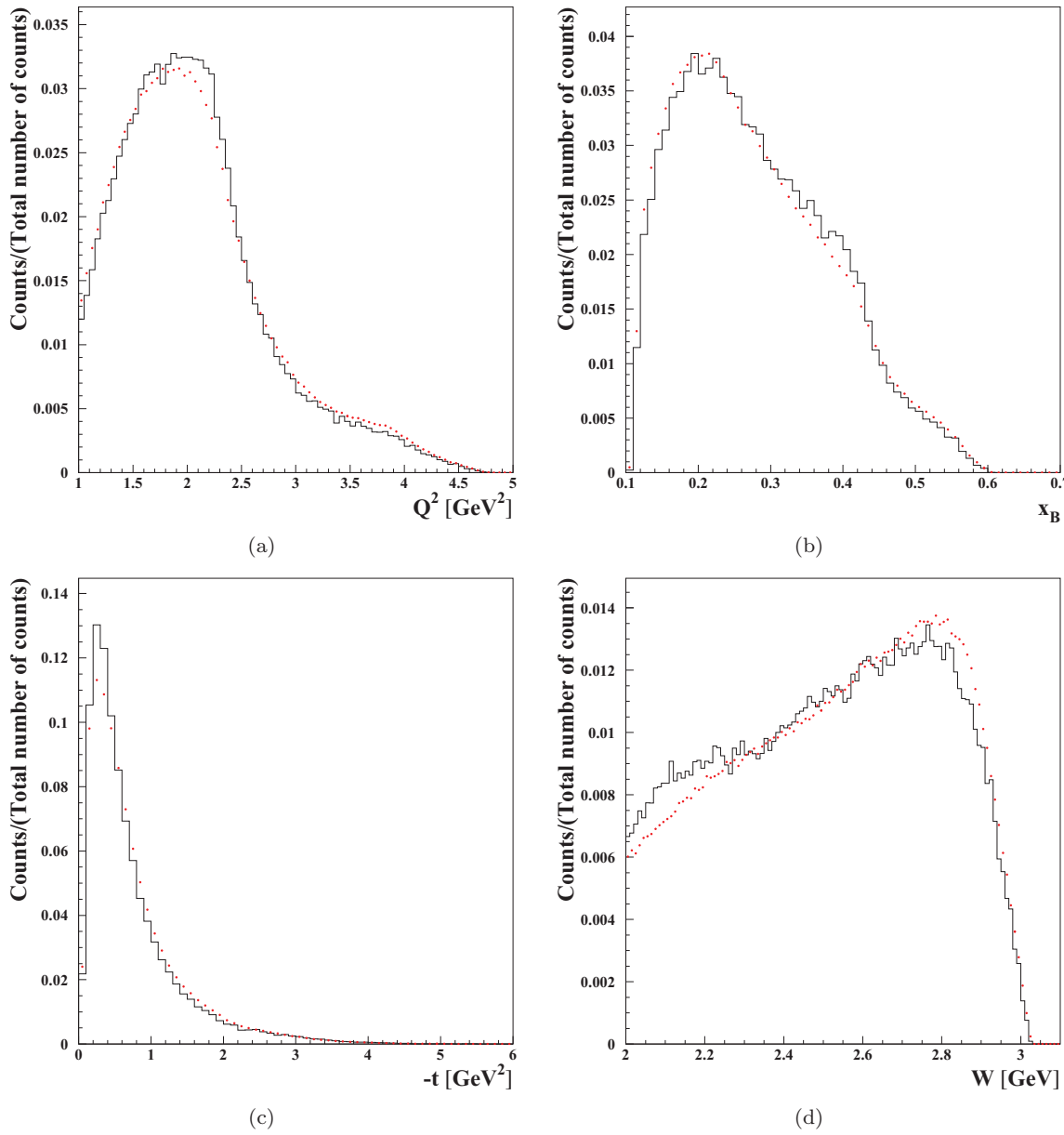

FIG. 7. (Color online) Distributions for kinematic variables Q^2 (a), x_B (b), $-t$ (c), and W (d) in arbitrary units. The data are in black (solid lines) and the results of Monte Carlo simulations are in red (dotted lines). The areas under the curves are normalized to each other.

the cluster area. As shown in Fig. 8, a $\pm 3.5\sigma$ sampling fraction cut was used in this analysis.

The distribution of the number of the photoelectrons in the CC is shown in Fig. 9. Figure 9(a) shows the distribution before the various cuts such as EC sampling fraction and angle and geometry matching between the electron track and the hits in the CC. The peak around $N_{\text{phe}} = 1$ represents the pion contamination. Figure 9(b) shows the same distribution after these cuts and the selection of the exclusive reaction (see Sec. IV B). The single photoelectron peak becomes negligibly small.

The charged-particle tracks were reconstructed by the DCs. The vertex location was calculated by the intersection of the track with the beam line. A cut was applied on the z component of the electron vertex position to eliminate events originating outside the target. The vertex distribution and cuts for one of the sectors are shown in Fig. 10. The left plot shows the z coordinate distribution before the exclusivity cuts, which are described below in Sec. IV B, and the right plot is the distribution after the exclusivity cuts. The peak at $z = -62.5$ cm exhibits the interaction of the beam with an insulating foil. It is completely removed after the exclusivity cuts, demonstrating that these cuts very effectively exclude the interactions involving nuclei of the surrounding nontarget material.

B. Proton identification

The proton was identified as a positively charged particle with the correct TOF. The quantity of interest ($\delta t = t_{\text{SC}} - t_{\text{exp}}$) is the difference in the time between the measured flight time from the event vertex to the SC system (t_{SC}) and that expected

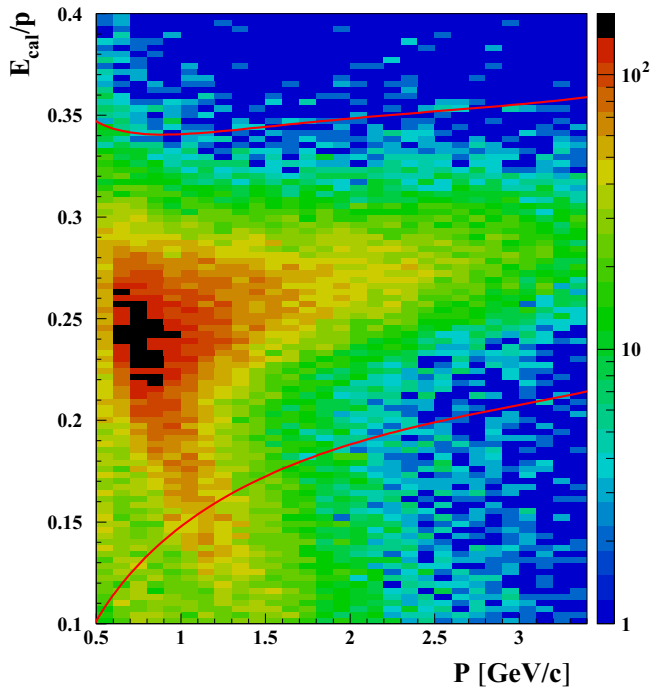

FIG. 8. (Color online) Sampling fraction $E_{\rm cal}/p$ of electrons in the EC as a function of electron momentum. The solid lines show the $\pm 3.5\sigma$ sampling-fraction cut used in this analysis.

for the proton ($t_{\rm exp}$). The quantity $t_{\rm exp}$ was computed from the velocity of the particle and the track length. The velocity was determined from the momentum assuming the mass of the particle equals that of a proton. A cut at the level of $\pm 5\sigma_t$ was applied around $\delta t = 0$, where σ_t is the TOF resolution. Such a wide cut is possible because the exclusivity cuts very effectively suppressed the remaining pion contamination.

C. Photon identification

Photons were detected in both calorimeters, the EC and the IC. In the EC, photons were identified as *neutral* particles with $\beta > 0.8$ and $E > 0.35$ GeV. Fiducial cuts were applied to avoid the EC edges. When a photon hits the boundary of the calorimeter, the energy cannot be fully reconstructed owing to the leakage of the shower out of the detector. Additional fiducial cuts on the EC were applied to account for the shadow of the IC (see Fig. 4). The calibration of the EC was done using cosmic muons and the photons from neutral-pion decay ($\pi^0 \to \gamma\gamma$).

In the IC each detected cluster was considered a photon. The assumption was made that this photon originated from the electron vertex. Additional geometric cuts were applied to remove low-energy clusters around the beam axis and photons near the edges of the IC, where the energies of the photons were incorrectly reconstructed owing to the electromagnetic shower leakage. The photons from $\pi^0 \to \gamma\gamma$ decays were detected in the IC in an angular range between 5° and 17° and in the EC for angles greater than 21°. The reconstructed invariant mass of two-photon events was then subjected to various cuts to isolate exclusive π^0 events, with a small residual background,

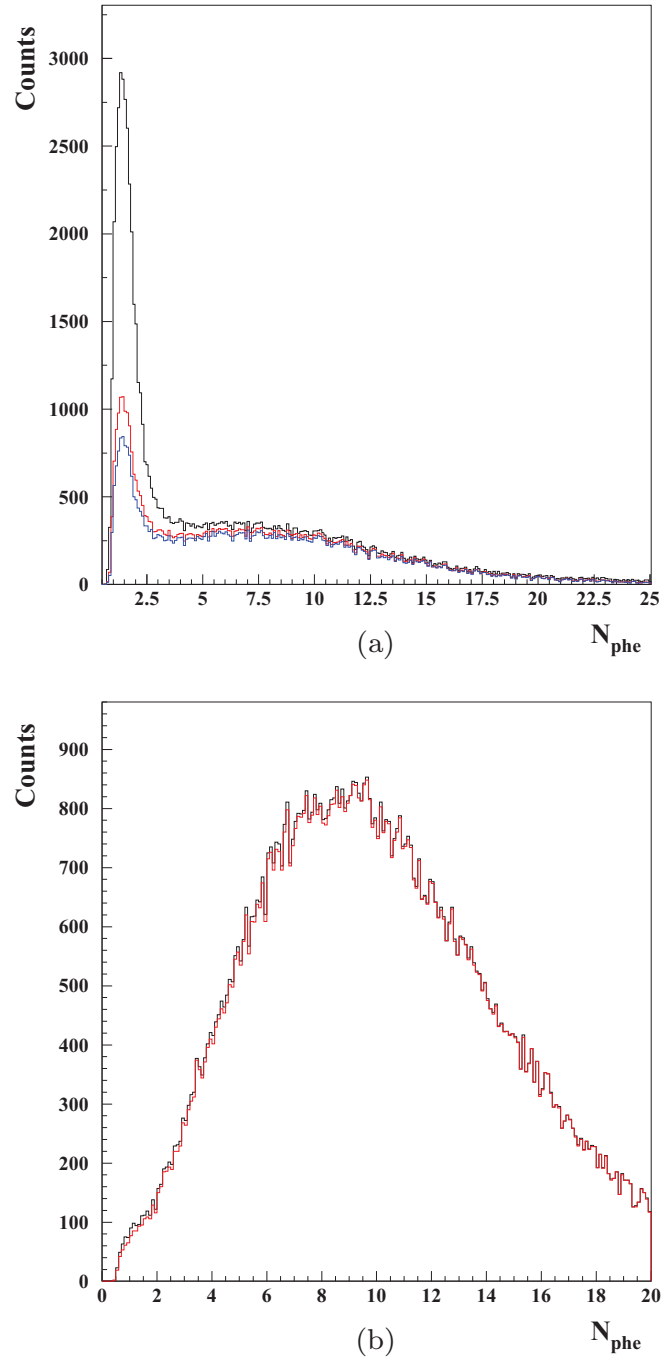

FIG. 9. (Color online) (a) The number of CC photoelectrons for events before the various cuts such as CC angle matching, EC sampling fraction, and exclusivity cuts were applied. (b) The number of CC photoelectrons for events that pass all cuts.

as discussed in the section on exclusivity cuts in Sec. IV B below.

D. Kinematic corrections

Ionization energy-loss corrections were applied to protons and electrons in both data and Monte Carlo events. These corrections were estimated using the GSIM Monte Carlo

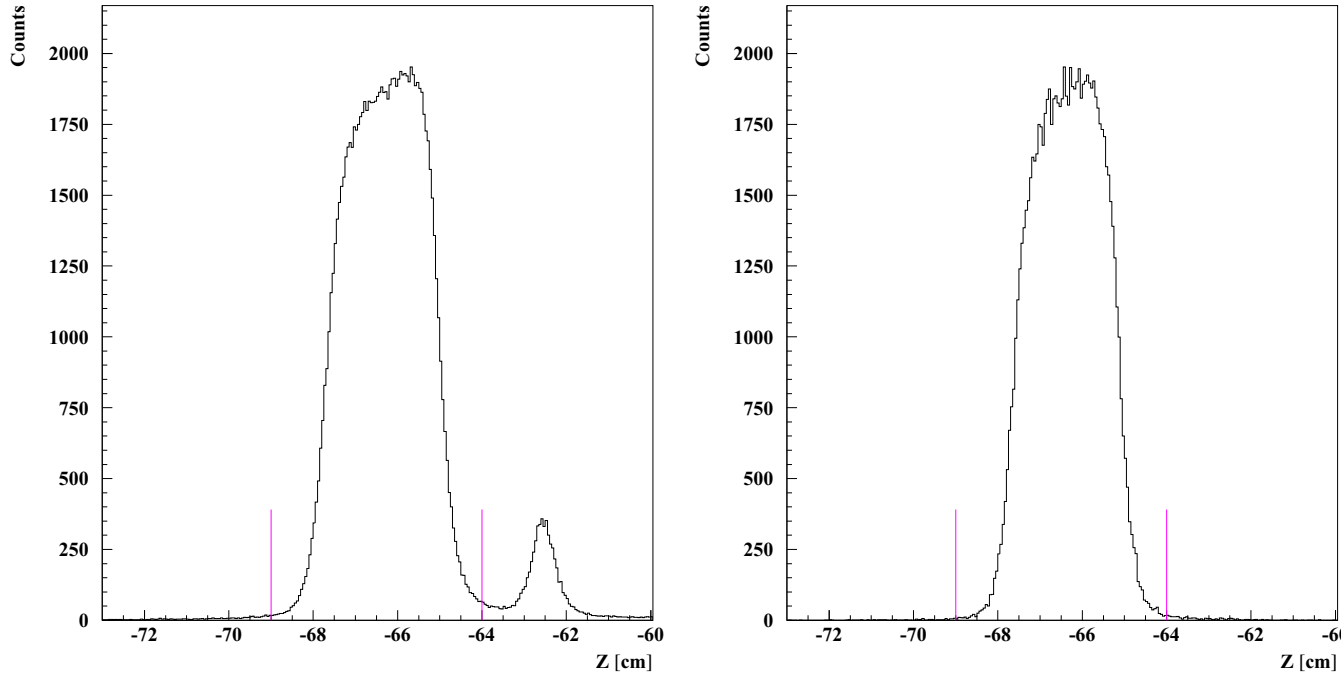

(a) Before exclusivity cuts (b) After exclusivity cuts

FIG. 10. (Color online) The z coordinate of the electron vertex. The vertical lines are the positions of the applied cuts. Note in (a) the small peak to the right of the target that is attributable to a foil placed at $z = -62.5$ cm downstream of the target window. In (b) the peak due to the foil is seen to disappear after the selection of the exclusive reaction.

program. Owing to imperfect knowledge of the properties of the CLAS detector, such as the magnetic-field distribution and the precise placement of the components or detector materials, small empirical sector-dependent corrections had to be made on the momenta and angles of the detected electrons and protons. The corrections were determined by systematically studying the kinematics of the particles emitted from well understood kinematically complete processes, e.g., elastic electron scattering. These corrections were on the order of 1%.

IV. EVENT SELECTION

A. Fiducial cuts

Certain areas of the detector acceptance were not efficient owing to gaps in the DC, problematic SC panels, and inefficient zones of the CC and the EC. These areas were removed from the analysis as well as the simulation by means of geometrical cuts, which were momentum, polar angle, and azimuthal angle dependent.

B. Exclusivity cuts

To select the exclusive reaction $ep \to e'p'\pi^0$, each event was required to contain an electron, one proton, and at least two photons in the final state. Then so-called *exclusivity cuts* were applied to all combinations of an electron, a proton, and two photons to ensure energy and momentum conservation, thus eliminating events in which there were any additional undetected particles.

Five cuts were used for the exclusive event selection (see Fig. 11):

(i) a cut, θ_X, on the angle between the reconstructed π^0 momentum vector and the missing momentum vector for the reaction $ep \to e'p'X$, in which $\theta_X < 2^\circ$;
(ii) the missing mass squared of the ep system ($ep \to e'p'X$), with $|M_x^2(ep) - M_{\pi^0}^2| < 3\sigma$;
(iii) the missing mass of the $e\gamma\gamma$ system ($ep \to e'\gamma\gamma X$), with $|M_x(e'\gamma\gamma) - m| < 3\sigma$;
(iv) the missing energy ($ep \to e'p'\gamma\gamma X$), with $|E_x(e'p\pi^0) - 0| < 3\sigma$;
(v) $\gamma\gamma$ invariant mass, $|M(\gamma\gamma) - M_{\pi^0}| < 3\sigma$.

Here σ is the observed experimental resolution obtained as the variance from the mean value of the distributions of each quantity. Three sets of resolutions were determined independently for each of the three photon-detection topologies (IC-IC, IC-EC, EC-EC). The effects of these cuts on the various distributions and the positions of the applied cuts are shown in Fig. 11 for the case where both photons were detected in the IC. These distributions were generally broader than in the Monte Carlo simulations so that the cuts for the data were typically broader than those used for the Monte Carlo simulations. Similar results were obtained for the topology in which one photon was detected in the IC and one in the EC, as well as the case where both photons were detected in the EC.

C. Background subtraction

The $M(\gamma\gamma)$ distribution contains a small amount of background under the π^0 peak even after the application

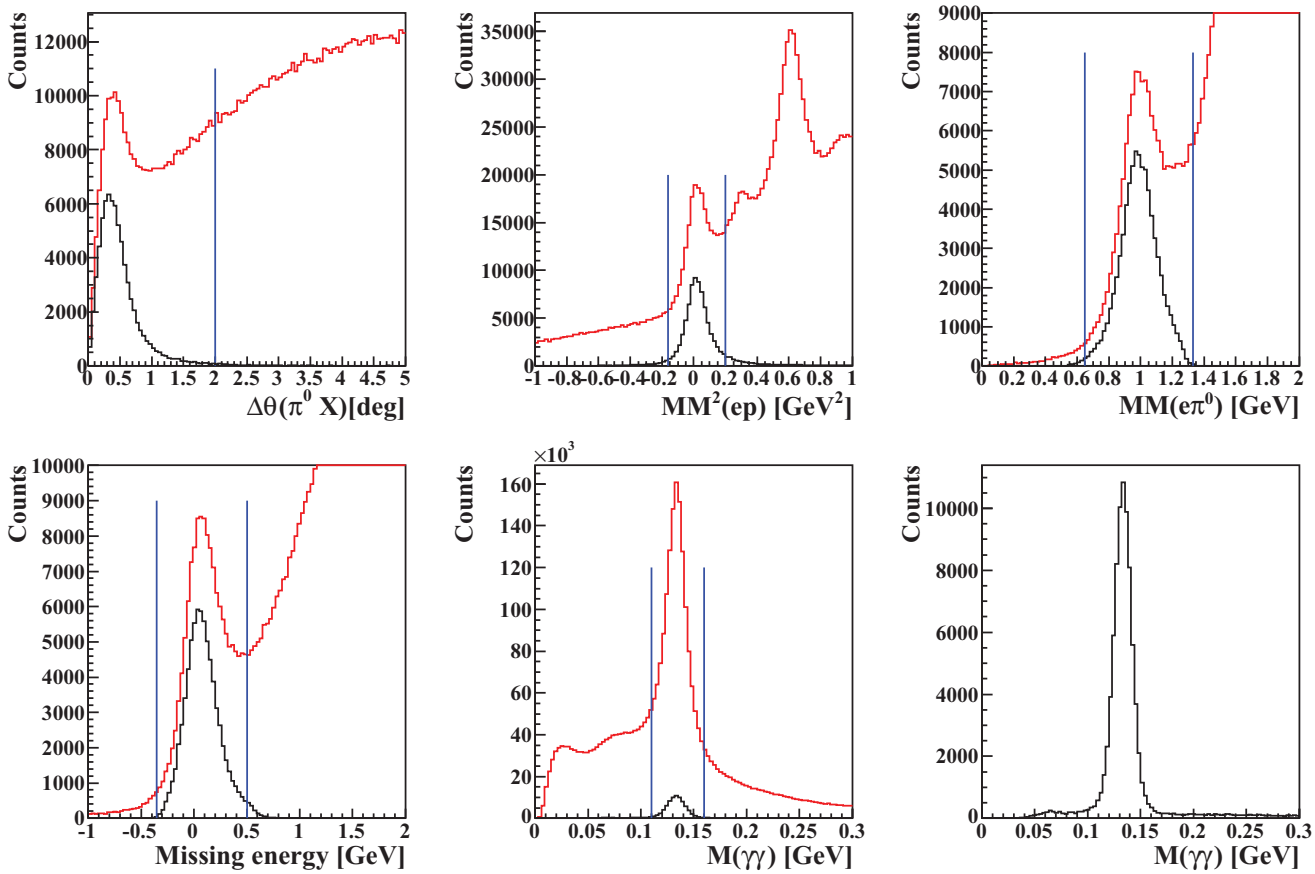

FIG. 11. (Color online) The exclusivity cuts for π^0 production for the topology where both decay photons are detected in the IC calorimeter. The graph for each variable shows the number of events per channel plotted before (red) and after (black) the cuts on the other variables. (Top left) θ_X cut: angle between the reconstructed π^0 momentum vector and the missing momentum vector $ep \to e'p'X$. (Top middle) Missing mass $M_X^2(ep)$. (Top right) Missing mass $M_X(e\gamma\gamma)$. (Bottom left) Missing energy $E_X(ep\gamma\gamma)$. (Bottom middle) Invariant mass $M(\gamma\gamma)$. (Bottom right) Same as in lower middle $[M(\gamma\gamma)]$, but magnified to illustrate the residual background. This background is subtracted from the pion distribution using the wings on either side of the peak, as explained in the text. The vertical lines denote the positions of the applied cuts on each distribution.

of all exclusivity cuts shown in Fig. 11. The background under the π^0 invariant mass peak, typically 3%–5%, was subtracted for each kinematic bin using the data in the sidebands $(-6\sigma,-3\sigma) \cup (3\sigma,6\sigma)$ in the $M(\gamma\gamma)$ distributions (bottom right distribution in Fig. 11 and in greater detail in Fig. 12). The same cuts were applied to all the kinematic bins.

D. Kinematic binning

The kinematics of the reaction are defined by four variables: Q^2, x_B, t, and ϕ_π. To obtain differential cross sections the data were divided into four-dimensional rectangular bins in these variables. There are 8 bins in x_B, Q^2, and t, as shown in Tables I–III. For each of these kinematic bins there are 20 bins in ϕ_π of equal angular width. The binning in x_B and Q^2 is shown in Fig. 6.

V. MONTE CARLO SIMULATION

The acceptance for each (Q^2, x_B, t, ϕ_π) bin of the CLAS detector with the present setup for the reaction $ep \to e'p'\gamma\gamma$ was calculated using the Monte Carlo program GSIM. The event generator used an empirical parametrization of the cross section as a function of Q^2, x_B, and t. The parameters were tuned using the MINUIT program to best match the simulated π^0 cross section with the measured electroproduction cross section. Two iterations were found to be sufficient to describe the experimental cross section and distributions. The comparisons of the experimental and Monte Carlo simulated distributions are shown in Fig. 7 for the variables Q^2, x_B, $-t$, and W.

Additional smearing factors for tracking and timing resolutions were included in the simulations to provide more realistic resolutions for charged particles. The Monte Carlo events were analyzed by the same code that was used to analyze the experimental data and with the additional smearing and somewhat different exclusivity cuts, to account for the leftover discrepancies in calorimeter resolutions. Ultimately, the number of reconstructed Monte Carlo events was an order of magnitude higher than the number of reconstructed experimental events. Thus, the statistical uncertainty introduced by the acceptance calculation was typically much smaller than the statistical uncertainty of the data.

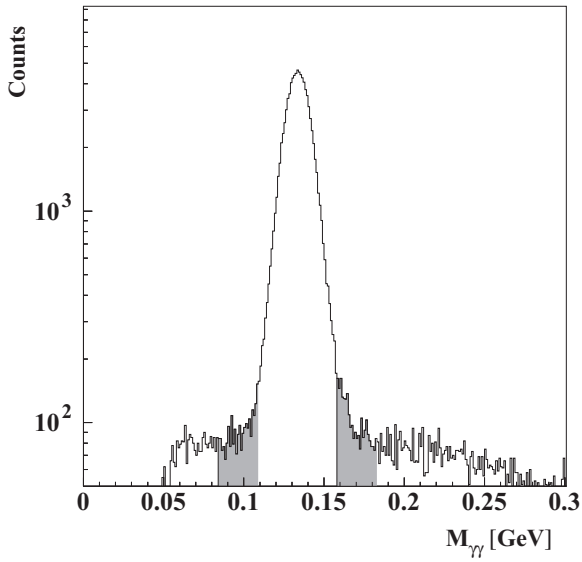

FIG. 12. The invariant mass distribution $M(\gamma\gamma)$ for all events in which all selection criteria were applied, where both decay photons were detected in the IC (note the log scale). The shaded regions were used to estimate the residual background on a kinematic bin-by-bin basis.

The efficiency of the event reconstruction depends on the level of noise in the detector: The greater the noise, the lower is the efficiency. It was found that the efficiency for reconstructing particles decreased linearly with increasing beam current. To take this into account, the background hits from random 3-Hz-trigger events were mixed with the Monte Carlo events for all detectors: DC, EC, IC, SC, and CC. The acceptance for a given bin i was calculated as a ratio of the number of reconstructed events to the number of generated events, including the random background events as

$$\epsilon_i(Q^2,x_B,t,\phi_\pi) = \frac{N_i^{\rm rec}(Q^2,x_B,t,\phi_\pi)}{N_i^{\rm gen}(Q^2,x_B,t,\phi_\pi)}. \quad (1)$$

Only areas of the four-dimensional space with an acceptance equal to or greater than 0.5% were used. This cut was applied to avoid the regions where the calculation of the acceptance was not reliable.

TABLE I. Q^2 bins.

Bin No.	Lower limit (GeV^2)	Upper limit (GeV^2)
1	1.0	1.5
2	1.5	2.0
3	2.0	2.5
4	2.5	3.0
5	3.0	3.5
6	3.5	4.0
7	4.0	4.6

TABLE II. x_B bins.

Bin No.	Lower limit	Upper limit
1	0.10	0.15
2	0.15	0.20
3	0.20	0.25
4	0.25	0.30
5	0.30	0.38
6	0.38	0.48
7	0.48	0.58

VI. RADIATIVE CORRECTIONS

Radiative processes which modify the observed cross section were taken into account. Some of these, illustrated in Fig. 13, include radiation of real photons, vacuum polarization, and lepton-photon vertex corrections. Vacuum polarization refers to the process where the virtual photon temporarily creates and annihilates a lepton-antilepton pair. The lepton-photon vertex corrections are for processes where a photon is emitted by the incoming electron and is absorbed by the outgoing electron. These processes give the largest contribution to the cross section at the next-to-leading-order level and can be calculated exactly from QED [26]. Thus, the measured cross section can be corrected to extract the Born term. The radiative correction, $\delta_{\rm RC}$, connects the experimentally measured cross section to the basic nonradiative (Born) cross section as follows:

$$\sigma_{\rm Born} = \frac{\sigma_{\rm meas}}{\delta_{\rm RC}}. \quad (2)$$

Here $\sigma_{\rm meas}$ is the observed cross section from experiment and $\sigma_{\rm Born}$ is the desired cross section after corrections.

The corrections were obtained using the software package EXCLURAD [26], which uses theoretical models as input for the hadronic current. The same analytical structure functions were implemented in the EXCLURAD package as were used to generate the π^0 electroproduction events in the Monte Carlo simulation. The corrections were computed for each kinematic bin (Q^2, x_B, t, ϕ_π). They vary from 5% to 10%, depending on the kinematics. For example, Fig. 14 shows the radiative corrections calculated for the first kinematic bin as a function of the ϕ_π angle. Note that the correction increases near $\phi_\pi = 0^\circ$ and $\phi_\pi = 360^\circ$.

TABLE III. $|t|$ bins.

Bin No.	Lower limit (GeV^2)	Upper limit (GeV^2)
1	0.09	0.15
2	0.15	0.20
3	0.20	0.30
4	0.30	0.40
5	0.40	0.60
6	0.60	1.00
7	1.00	1.50
8	1.50	2.00

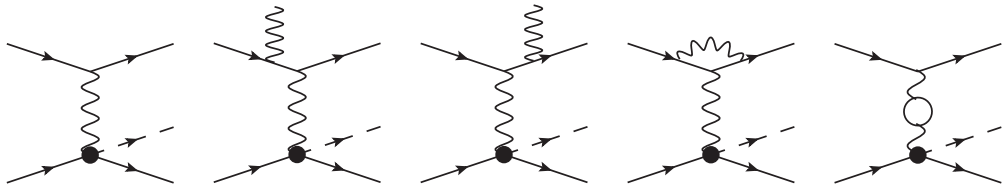

FIG. 13. Feynman diagrams contributing to the pion electroproduction cross section. (Left to right) Born process, bremsstrahlung (by the initial and the final electron), vertex correction, and vacuum polarization.

VII. NORMALIZATION CORRECTION

To check the overall absolute normalization the cross section of elastic electron-proton scattering was measured using the same data set. The measured cross section was lower than the known elastic cross section by approximately 12% over most of the elastic kinematic range. Studies made using additional other reactions where the cross sections are well known, such as π^0 production in the resonance region, and Monte Carlo simulations of the effects of random backgrounds, indicate that this was approximately true over a wide range of kinematics. Thus, a normalization factor $\delta_{\rm Norm} \sim 0.89$ was applied to the measured cross section. This value includes the efficiency of the SC counters, which was estimated to be around around 95%, as well as other efficiency factors which are not accounted for in the analysis, such as trigger and CC efficiency effects. This correction comprises the largest single contribution to the systematic uncertainties in the extracted cross section.

VIII. SYSTEMATIC UNCERTAINTIES

The determination of the differential cross section of the reaction $ep \to e'p'\pi^0$ requires the knowledge of the yield and the acceptance, including various efficiency factors and radiative effects, for each kinematic bin (Q^2,x_B,t,ϕ_π), as well as the integrated luminosity of the experiment. These quantities are subject to systematic uncertainties which contribute to the uncertainty of the measured cross section in each kinematic bin. Each of these factors is subject to systematic uncertainty. The size of these systematic uncertainties was estimated by repeating the calculation of the cross section, varying each of the cut parameters within reasonable limits. Table IV contains a summary of the information on all the studied sources of systematic uncertainties. Some sources of uncertainty vary bin by bin; others are global.

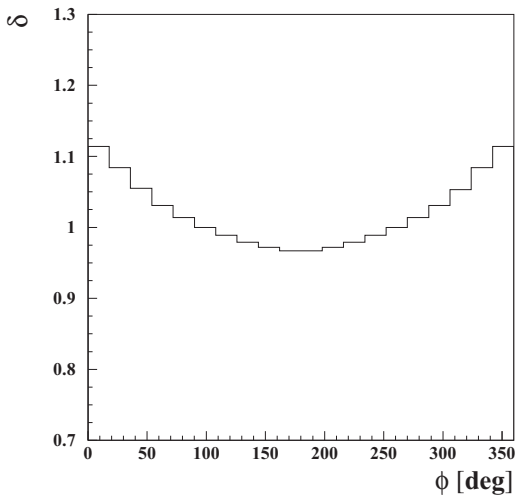

FIG. 14. Radiative corrections for π^0 electroproduction as a function of ϕ_π for the bin ($Q^2 = 1.25$ GeV^2, $x_B = 0.125$, $t = -0.12$ GeV^2).

The systematic uncertainty on the proton identification was studied by removing the cut on the difference between the measured and predicted flight times. The systematic uncertainty was estimated in each (Q^2,x_B,t,ϕ_π) bin to be, on average, ~2.5%.

To estimate the systematic uncertainty introduced by the electron and proton fiducial cuts, we varied the cuts applied to the ϕ angles accepted in each sector. The ϕ acceptance of each of the six sectors was less than 60°, depending on θ, owing to the thickness of the toroid magnet coil cryostats. To avoid tracks which are too close to the coils, a fiducial cut in $\Delta\phi$ was applied of nominally 40° (±20° from the sector midplane) at larger angles θ, tapering down to smaller $\Delta\phi$ for smaller θ as the ϕ acceptance decreases. For electrons, an additional cut of ±3° from the midplane was applied to avoid known inefficiencies of the Cherenkov detector in the sector midplane. The average systematic uncertainty arising from the placement of these cuts was estimated to be around 4.7%.

The lower limit on the photon's energy in the EC calorimeter was varied from 350 to 300 MeV for the evaluation of the systematic uncertainties owing to this selection criteria. The uncertainties were calculated for each bin and, on average, were estimated to be ~1.6%.

The systematic uncertainties owing to the exclusivity cuts on $M_x(e\gamma\gamma)$, $E_x(ep\pi^0)$, and $M(\gamma\gamma)$ were studied in detail for each cut independently. The cuts were changed from 3σ to 2σ and systematic uncertainties were calculated in each bin. The average uncertainties for each cut, shown in Table IV, varied between 2.5% and 3.2%.

The systematic uncertainty of the radiative corrections was estimated as follows. The missing mass of the ep system $M_x(ep)$ exhibits a radiative tail. Thus, when making a cut on $M_x(ep)$ there is a loss of radiated events, which was corrected using the routine EXCLURAD [26], which depends on the value of the cut. The correction procedure was applied with varied cuts on $M_x(ep)$ from 0.1 to 0.25 GeV in the data analysis program, and the same value of this cut was applied to the simulated data. The obtained cross sections were compared to the original ones bin by bin. On average, the uncertainty was estimated to be 2.9%.

TABLE IV. Summary table of systematic uncertainties. B denotes bin-to-bin and O indicates overall uncertainties.

Source	Bin-to-bin or overall	Average uncertainty (%)
Proton ID	B	~2.5
Fiducial cut	B	~4.7
Cut on energy of photon detected in the EC	B	~1.6
Cut on missing mass of the $e'\gamma\gamma$	B	~2.5
Cut on invariant mass of 2 photons	B	~2.9
Cut on missing energy of the $ep'\gamma\gamma$	B	~3.2
Radiative corrections	B	~2.9
Total beam charge on target	O	<1
Target length	O	0.2
Absolute normalization	O	6.0

The systematic uncertainty in the cross section owing to the normalization correction factor was estimated by the comparison of the normalization factors extracted from the six independent measurements of the elastic cross section in the six different CLAS sectors. The absolute normalization correction reflects systematic uncertainties which were not accounted for and which may lead to normalization errors. This systematic uncertainty was estimated to be 6%.

The uncertainty in the incident electron beam energy was determined to be about 0.017 GeV and its contribution to the overall cross section is small.

Finally, the overall systematic uncertainty was estimated by adding all contributions in quadrature and is about 10%.

IX. CROSS SECTIONS FOR $\gamma^* p \to \pi^0 p$

The fourfold differential cross section as a function of the four variables (Q^2, x_B, t, ϕ_π) was obtained from the expression

$$\frac{d^4\sigma_{ep\to e'p'\pi^0}}{dQ^2 dx_B dt d\phi_\pi} = \frac{N(Q^2,x_B,t,\phi_\pi)}{\mathcal{L}_{\rm int}(\Delta Q^2 \Delta x_B \Delta t \Delta\phi_\pi)} \times \frac{1}{\epsilon_{\rm ACC}\delta_{\rm RC}\delta_{\rm Norm}{\rm Br}(\pi^0\to\gamma\gamma)}. \quad (3)$$

The definitions of the kinematic variables are given in Appendix A. The definitions of the other quantities in Eq. (3) are as follows.

(i) $N(Q^2, x_B, t, \phi_\pi)$ is the number of $ep \to e'p'\pi^0$ events in a given (Q^2, x_B, t, ϕ_π) bin.

(ii) $\mathcal{L}_{\rm int}$ is the integrated luminosity (which takes into account the correction for the data-acquisition dead time).

(iii) $(\Delta Q^2 \Delta x_B \Delta t \Delta\phi_\pi)$ is the corresponding bin width (see Tables I–III). For bins not completely filled, because of cuts in θ_e, W, and E', as seen in Fig. 6, the phase space $(\Delta Q^2 \Delta x_B \Delta t \Delta\phi_\pi)$ includes a four-dimensional correction to take this into account. The specified Q^2, x_B, and t values are the mean values of the data for each variable for each four-dimensional bin, as if the cross sections in each bin vary linearly in each variable in the filled portion of the accepted kinematic volume.

(iv) $\epsilon_{\rm ACC}$ is the acceptance calculated for each bin (Q^2, x_B, t, ϕ_π).

(v) $\delta_{\rm RC}$ is the correction factor owing to the radiative effects calculated for each (Q^2, x_B, t, ϕ_π) bin.

(vi) $\delta_{\rm Norm}$ is the overall absolute normalization factor calculated from the elastic cross section measured in the same experiment (see Sec. VIII above).

(vii) ${\rm Br}(\pi^0 \to \gamma\gamma) = \frac{\Gamma(\pi^o\to\gamma\gamma)}{\Gamma_{\rm total}}$ is the branching ratio for the $\pi^0 \to \gamma\gamma$ decay mode.

The reduced or "virtual photon" cross sections were extracted from the data through

$$\frac{d^2\sigma_{\gamma^* p\to p'\pi^0}(Q^2,x_B,t,\phi_\pi,E)}{dt d\phi_\pi} = \frac{1}{\Gamma_V(Q^2,x_B,E)} \frac{d^4\sigma_{ep\to e'p'\pi^0}}{dQ^2 dx_B dt d\phi_\pi}. \quad (4)$$

The Hand convention [27] was adopted for the definition of the virtual-photon flux Γ_V [see Eq. (B2) in Appendix B]. A table of the 1867 reduced cross sections can be obtained online in the Supplemental Material, Ref. [28]. As an example of the information available, Table V presents the reduced cross section for one kinematical point ($Q^2 = 1.15$ GeV^2, $x_B = 0.132$, $t = -0.12$ GeV^2).

A. Integrated virtual-photon cross section $\sigma_U = \sigma_T + \epsilon\sigma_L$

The total virtual-photon cross section is defined as the reduced differential cross section integrated over ϕ_π and t,

$$\sigma_U = \sigma_T + \epsilon\sigma_L = \iint \frac{d^2\sigma}{dt d\phi_\pi} dt d\phi_\pi, \quad (5)$$

where σ_T and σ_L are attributable to transverse and longitudinal photons respectively. σ_U depends on two variables Q^2 and x_B. The variable ϵ is the ratio of fluxes of longitudinally and transversely polarized virtual photons [see Eq. (B3) in Appendix B].

Because the CLAS acceptance has limited coverage in some areas of the four-dimensional phase space (Q^2, x_B, t, ϕ_π), the integral could be carried out over a finite range of the total phase space. For example, at high Q^2 and x_B, the acceptance around $\phi_\pi = 180^\circ$ is near zero, so the ϕ_π integral cannot be fully calculated using the present data. To account for regions with small acceptance, a model that was developed for the

TABLE V. $d^2\sigma/dtd\phi_\pi$ at $t = -0.18$ GeV^2, $x_B = 0.22$, and $Q^2 = 1.75$ GeV^2. The complete numerical listing for all measured kinematic points is found in Ref. [28].

ϕ_π (deg)	$\frac{d^2\sigma}{dtd\phi_\pi}$ (nb/GeV^2)	Statistical error (nb/GeV^2)	Systematic error (nb/GeV^2)
9	55.8	9.0	12.0
27	45.5	6.1	0.7
45	56.7	5.9	6.0
63	62.0	6.3	6.6
81	70.8	6.1	11.1
99	85.2	6.5	7.0
117	61.7	6.4	5.8
135	41.2	5.9	4.6
153	35.7	5.5	3.6
171	44.8	7.8	0.5
189	30.9	5.9	3.6
207	41.0	5.9	5.6
225	42.9	6.5	2.8
243	51.8	5.8	8.8
261	69.2	6.0	2.4
279	82.3	7.3	3.6
297	77.5	7.1	4.2
315	57.8	5.5	9.8
333	48.7	6.2	4.4
351	37.3	7.8	8.2

Monte Carlo generator to describe $d^2\sigma^{\rm MC}/dtd\phi_\pi$ was used. This generator was tuned using our own π^0 experimental data. Thus, the integrated cross sections have an additional factor $1/\eta$, where

$$\eta = \frac{\int\int_{\Omega'} \frac{d^2\sigma^{\rm MC}}{dtd\phi_\pi} dtd\phi_\pi}{\int\int_{\Omega} \frac{d^2\sigma^{\rm MC}}{dtd\phi_\pi} dtd\phi_\pi}, \tag{6}$$

in which Ω is the full phase space and Ω' is the phase space where CLAS has nonzero acceptance. Only data points were included for partially covered kinematic volumes in which η was greater than 0.45 to avoid extrapolation to the regions where the acceptance is low. The value of η is model dependent, which introduces an additional systematic uncertainty of $\sim$15%. The integration over the variable $|t|$ extends from $|t_{\rm min}|$ to 2 GeV^2.

The results have been found to be consistent with the results of Ref. [14], which reported high accuracy cross sections near the lower Q^2, W, and $|t|$ regions of the present experiment.

Figure 15 shows the integrated cross section σ_U as a function of Q^2 for different values of x_B. The cross sections were fit by the simple expression $\sigma_U \sim 1/Q^n$ to estimate the Q^2 dependence. The weighted mean of the exponent parameters is $n = 4.7 \pm 0.7$. Reference [14] finds $n = 4.78 \pm 0.16$ based upon two values of Q^2 (1.9 and 2.3 GeV^2). The asymptotic prediction of the conventional GPD models is $\sigma_L \sim 1/Q^6$ and $\sigma_T \sim 1/Q^8$. The parameters of the fit are given in Table VI.

The total cross section $\sigma_U = \sigma_T + \epsilon\sigma_L$ as a function of W for different values of Q^2 is shown in Fig. 16. The cross sections were fitted with the function $\sigma \sim 1/W^n$. The weighted mean value of the exponent is $n = 3.7 \pm 0.3$. Reference [14] finds $n = 3.48 \pm 0.11$ based upon two values of W. The W dependence is consistent with what was observed for ρ electroproduction [29]; i.e., the cross section decreases with W compatibly with the Regge-model predictions [20] for the exclusive reactions. The parameters of the fit are given in Table VII.

B. The t-dependent differential cross section $d\sigma_U/dt$

Integrating only over ϕ_π yields the t-dependent differential cross section

$$\frac{d\sigma_U}{dt} = \int \frac{d^2\sigma}{dtd\phi_\pi} d\phi_\pi. \tag{7}$$

The correction factor for the region where the CLAS detector has zero acceptance was calculated as

$$\eta' = \frac{\int_{\Omega^*} \frac{d^2\sigma^{\rm MC}}{dtd\phi} d\phi_\pi}{\int_{\Omega} \frac{d^2\sigma^{\rm MC}}{dtd\phi_\pi} d\phi_\pi}, \tag{8}$$

in which Ω is the full phase space and Ω^* is the phase space where CLAS has nonzero acceptance.

Figure 17 shows the cross section $d\sigma_T/dt + \epsilon d\sigma_L/dt$ for intervals of Q^2 for the different values of x_B. The presented cross sections were calculated only for the kinematics where the factor η' was greater than 0.45. The general feature of these distributions is that in a small interval near $|t| = |t|_{\rm min}$ they are not diffractive. There, the cross sections cannot be described by simple exponential functions. However, for somewhat larger values of $|t|$, the cross sections appear to fall off exponentially with $-t$, and thus were fit by the function e^{bt}, where the exponential functions appear to fit the data with a good χ^2. This provides a qualitative description of the $|t|$ dependence by a slope parameter b. The curves in Fig. 17 are the results of these fits.

Figure 18 shows the slope parameter b as a function of x_B for different values of Q^2. The values of b are between 1 and 2.5 GeV^{-2}. The data appear to exhibit a slope parameter decrease with increasing x_B for each Q^2 over much of the measured range, except at the highest measured regions of x_B and Q^2. However, the $Q^2 - x_B$ correlation in the CLAS acceptance does not permit one to make a definite conclusion about the Q^2 dependencies of the slope parameter for fixed x_B. What one can say is that at high Q^2 and high x_B ($Q^2 = 4.3$ GeV^2, $x_B = 0.53$), the slope parameter is smaller than for the lowest values of these variables ($Q^2 = 1.2$ GeV^2, $x_B = 0.12$). The b parameter in the exponential determines the width of the transverse momentum distribution of the emerging protons, which, by a Fourier transform, is inversely related to the transverse size of the interaction region from which the proton emerges. From the point of view of the handbag picture, it is inversely related to the separation, $r_\perp$, between the active quark and the center of momentum of the spectators (see Ref. [30]). Thus, the data imply that the separation is larger at the lowest x_B and Q^2 and becomes smaller for increasing x_B and Q^2, as it must.

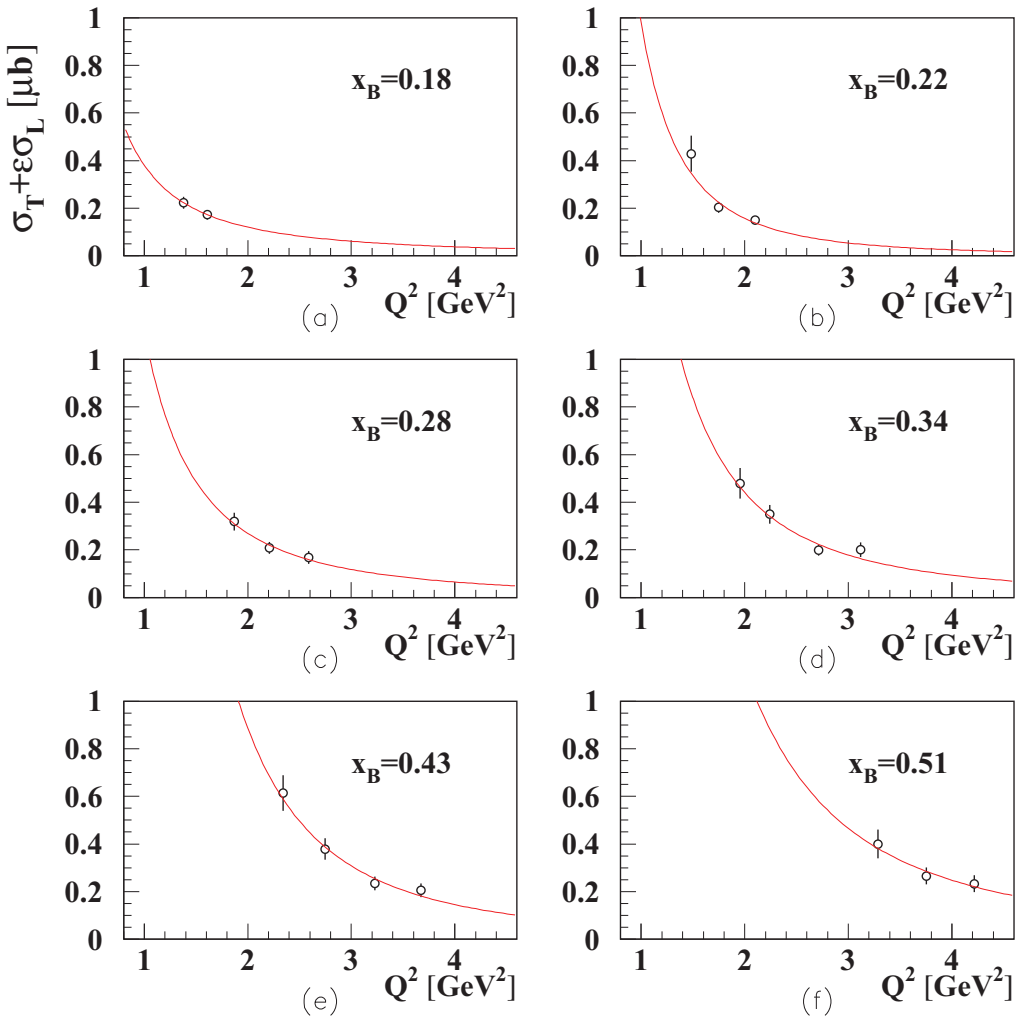

FIG. 15. (Color online) The t-integrated "virtual photon" cross section $\sigma_T + \epsilon\sigma_L$ as a function of Q^2 for the reaction $\gamma^* p \to p'\pi^0$ for $x_B = 0.18, 0.22, 0.28, 0.34, 0.43$, and 0.51. The curves are fits to a power law $\sigma_U = A_{Q^2}/Q^n$, where A_{Q^2} and n are fit parameters.

C. Structure functions

The reduced cross sections can be expanded in terms of structure functions $d\sigma_T/dt$, $d\sigma_L/dt$, $d\sigma_{LT}/dt$, and $d\sigma_{TT}/dt$ as

$$\frac{d^2\sigma}{dtd\phi_\pi} = \frac{1}{2\pi}\left[\left(\frac{d\sigma_T}{dt} + \epsilon\frac{d\sigma_L}{dt}\right) + \epsilon\cos 2\phi_\pi \frac{d\sigma_{TT}}{dt} + \sqrt{2\epsilon(1+\epsilon)}\cos\phi_\pi \frac{d\sigma_{LT}}{dt}\right], \quad (9)$$

TABLE VI. Parameters of Q^2-dependent fits to the t-integrated cross sections in Fig. 15 for different values of x_B.

x_B	A_{Q^2}	n
0.18	0.38 ± 0.16	3.32 ± 2.04
0.22	0.97 ± 0.39	5.26 ± 1.34
0.28	1.11 ± 0.48	4.09 ± 1.12
0.34	2.06 ± 0.71	4.46 ± 0.77
0.43	5.41 ± 1.83	5.22 ± 0.63
0.51	5.19 ± 3.12	4.39 ± 0.91

from which the three combinations of structure functions, $(\frac{d\sigma_T}{dt} + \epsilon\frac{d\sigma_L}{dt})$, $\frac{d\sigma_{TT}}{dt}$, and $\frac{d\sigma_{LT}}{dt}$ can be extracted by fitting the cross sections to the ϕ_π distribution in each bin of (Q^2, x_B, t). The decomposition of the structure functions in terms of helicity amplitudes is given in Appendix B, Eqs. (B10) to (B13).

The physical significance of the structure functions is as follows.

(i) $d\sigma_L/dt$ is the sum of structure functions initiated by a longitudinal virtual photon, both with and without nucleon helicity-flip, i.e., respectively, $\Delta\nu = \pm 1$ and $\Delta\nu = 0$.

(ii) $d\sigma_T/dt$ is the sum of structure functions which are initiated by a transverse virtual photon of positive and negative helicity ($\mu = \pm 1$), with and without nucleon helicity flip, respectively $\Delta\nu = \pm 1$ and 0.

(iii) $d\sigma_{LT}/dt$ corresponds to interferences involving products of amplitudes for longitudinal and transverse photons.

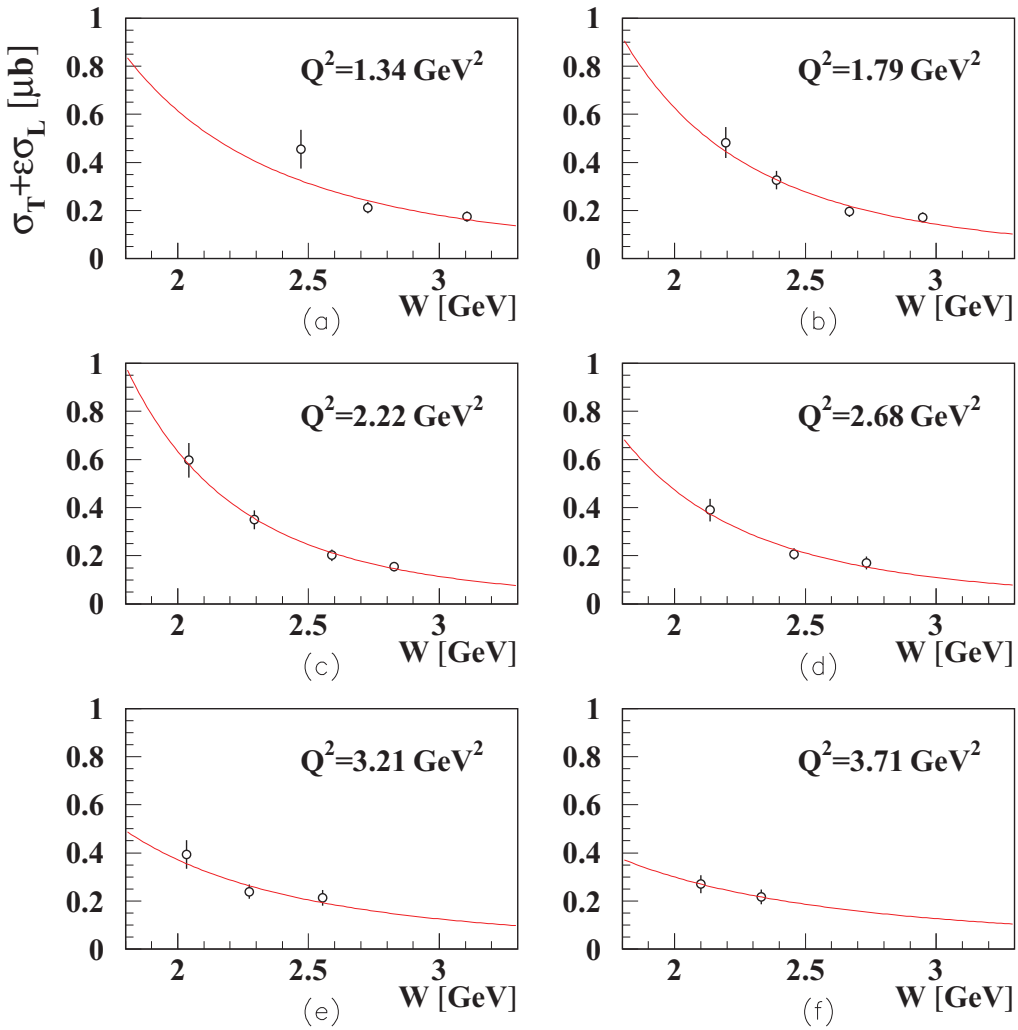

FIG. 16. (Color online) The t-integrated "virtual photon" cross section $\sigma_T + \epsilon\sigma_L$ as a function of W for the reaction $\gamma^* p \to p'\pi^0$ for $Q^2 = 1.34$, 1.79, 2.22, 2.68, 3.21, and 3.71 GeV^2. The curves are fits to a power law $\sigma_U = A_W / W^n$, where A_W and n are fit parameters.

(iv) $d\sigma_{TT}/dt$ corresponds to interferences involving products of transverse positive and negative photon helicity amplitudes.

Figure 19 shows a typical ϕ_π distribution of the virtual-photon cross sections with a fit using the form of Eq. (9). These data are listed in Table V as well. The complete listing of all differential cross sections for all kinematic settings are found in Ref. [28].

TABLE VII. Parameters of W-dependent fits to the t-integrated cross sections in Fig. 16 for different values of Q^2.

Q^2	A_W	n
1.34	5.01 ± 2.94	3.03 ± 0.56
1.79	7.82 ± 2.77	3.64 ± 0.37
2.22	11.90 ± 3.53	4.23 ± 0.33
2.68	5.76 ± 2.64	3.61 ± 0.52
3.21	2.38 ± 1.56	2.68 ± 0.80
3.71	1.30 ± 1.24	2.12 ± 1.20

Figure 20 shows the extracted structure functions for all kinematical bins in (Q^2, x_B, t). The values of the structure functions are given numerically in Table VIII. The results of a Regge-based calculation [20] are also shown in Fig. 20.

A number of observations can be made independently of the model predictions. The $d\sigma_{TT}/dt$ structure function is negative and $|d\sigma_{TT}/dt|$ is comparable in magnitude with the unpolarized structure function $(d\sigma_T/dt + \epsilon d\sigma_L/dt)$. However, $d\sigma_{LT}/dt$ is small in comparison with $d\sigma_U/dt$ and $d\sigma_{TT}/dt$. This reinforces the conclusion that the asymptotic leading-order handbag approach for which $d\sigma_L/dt$ is dominant is not applicable at the present values of Q^2.

X. COMPARISONS WITH THEORETICAL MODELS

A. Regge model

The Regge model with charge exchange and $\pi^\pm$ final-state interactions, in addition to pole terms and elastic π^0 rescattering, had been successfully applied in Refs. [31,32] to π^0 electroproduction at DESY at $Q^2 = 0.25$, 0.50, and 0.85 GeV^2. This mechanism, which is illustrated schematically

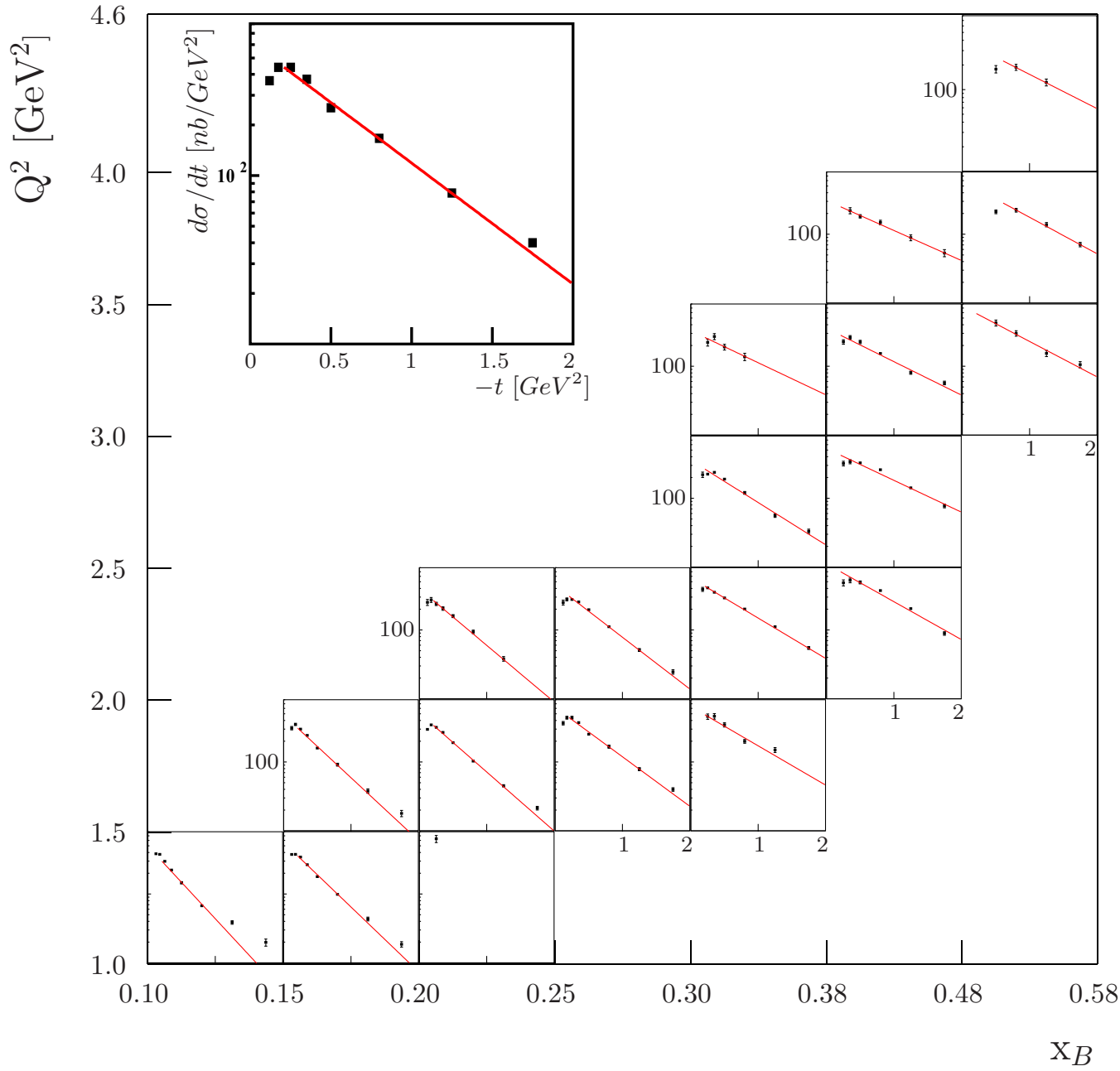

FIG. 17. (Color online) The differential cross section $d\sigma_U/dt = d\sigma_T/dt + \epsilon d\sigma_L/dt$ for the reaction $\gamma^* p \to p'\pi^0$. The curves are fits to the exponential function e^{bt}. The inset is an enlarged copy of the panel centered at $Q^2 = 1.75$ GeV^2 and $x_B = 0.275$. Systematic uncertainties, including the estimated systematic uncertainty in the integration correction factor η of 15%, as discussed in the text, are not shown.

in Fig. 21, includes a charged-pion rescattering amplitude (see Fig. 22). Schematically, the amplitude can be written as a product of two terms,

$$T_{\pi N} \propto \int d\Omega T_{\gamma p \to \pi^+ N}(t_\gamma) T_{\pi N \to \pi^0 p}(t_\pi),$$

in which $t_\gamma = (k_\gamma - P_\pi)^2$. The first term in the integral is the amplitude for production of a charged off-shell meson by a virtual photon, and the second characterizes its rescattering. The amplitudes are largest where the intermediate mesons become on shell.

However, when this scheme was applied to the Jefferson Lab Hall A kinematics [14] at $Q^2 = 2.35$ GeV^2, the calculated cross sections were found to be an order of magnitude too low (see Ref. [20]). In fact, it was very difficult to understand why the experimental cross section at $Q^2 = 2.35$ GeV^2 is comparable in magnitude to the cross section at much lower Q^2 values.

Then Ref. [20] included a vector-meson rescattering amplitude (see Fig. 22) taking the form

$$T_{VN} \propto \int d\Omega T_{\gamma p \to VN}(t_\gamma) T_{VN \to \pi^0 p}(t_\pi).$$

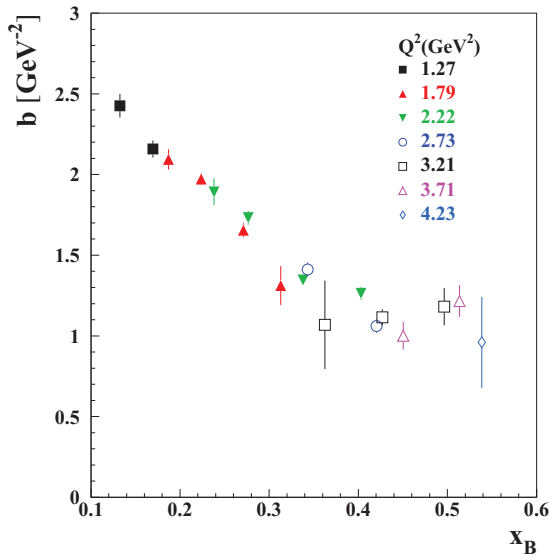

FIG. 18. (Color online) t-slope parameter b for the reaction $\gamma^* p \to p'\pi^0$ as a function of x_B for different values of Q^2.

It was found that the contributions of the $\rho^+\Delta^0$ and $\rho^-\Delta^{++}$ rescattering (Fig. 22, bottom right) are the most important, far more important than the ωp or $\rho^0 p$ terms because the cross section of the $N(\rho^+,\pi)N$ reaction is larger than the $N(\omega,\pi)N$ cross section, and $N(\rho^0,\pi^0)N$ cannot occur. These comparisons were only carried out in a narrow range of kinematics corresponding to the available Hall A data.

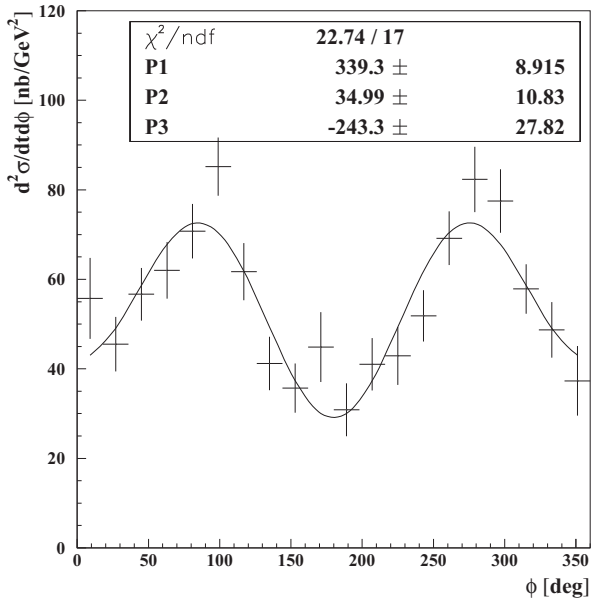

FIG. 19. Example of the ϕ_π distribution of $d^2\sigma/dtd\phi_\pi$. The solid curve is a fit of the function in Eq. (9). The kinematic bin corresponding to this figure is at $t = -0.18$ GeV^2, $x_B = 0.22$, and $Q^2 = 1.75$ GeV^2 and the data are listed in Table V. Error bars are statistical. The complete listing of all differential cross sections for all kinematic settings are found in Ref. [28].

The comparison of the present data with the predictions of the Regge model [20] is shown in Fig. 20. Although the Regge model managed to describe the Hall A cross-section data in a narrow region of Q^2 and t, the situation here, with the large kinematic acceptance, is much more complex. In some regions of Q^2 and t the predictions appear better than in others. This model does predict the correct signs and values of σ_{TT} and the small value of σ_{LT} in almost all the data intervals.

B. Handbag model

Figure 23 shows the experimental structure functions at selected values of Q^2 and x_B. The results of two GPD-based models which include transversity GPDs [18,19] are superimposed in Fig. 23. The primary contributing GPDs in meson production for transverse photons are H_T, which characterizes the quark distributions involved in nucleon helicity flip, and $\bar{E}_T(=2\widetilde{H}_T + E_T)$, which characterizes the quark distributions involved in nucleon helicity-nonflip processes [33,34]. As a reminder, in both cases the active quark undergoes a helicity flip.

Reference [18] obtains the following relations (see the Appendix for more details):

$$\frac{d\sigma_T}{dt} = \frac{4\pi\alpha}{2k'}\frac{\mu_\pi^2}{Q^8}\left[(1-\xi^2)|\langle H_T\rangle|^2 - \frac{t'}{8m^2}|\langle \bar{E}_T\rangle|^2\right], \quad (10)$$

$$\frac{d\sigma_{TT}}{dt} = \frac{4\pi\alpha}{k'}\frac{\mu_\pi^2}{Q^8}\frac{t'}{16m^2}|\langle \bar{E}_T\rangle|^2. \quad (11)$$

Here $\kappa'(Q^2,x_B)$ is a phase space factor, $t' = t - t_{\min}$, where $|t_{\min}|$ is the minimum value of $|t|$ corresponding to $\theta_\pi = 0$, and the brackets $\langle H_T\rangle$ and $\langle \bar{E}_T\rangle$ denote the convolution of the elementary process with the GPDs H_T and $\bar{E}_T$. The GPD $\bar{E}_T$ describes the spatial density of transversely polarized quarks in an unpolarized nucleon [33,34].

Note that for the case of nucleon helicity-nonflip, characterized by the GPD $\bar{E}_T$, overall helicity from the initial to the final state is not conserved. However, angular momentum is conserved, the difference being absorbed by the orbital motion of the scattered π^0-N pair. This accounts for the additional $t'(=t - t_{\min})$ factor multiplying the $\bar{E}_T$ terms in Eqs. (10) and (11).

In both calculations the contribution of σ_L accounts for only a small fraction (typically less than a few percent) of the unseparated structure functions $d\sigma_T/dt + \epsilon d\sigma_L/dt$ in the kinematic regime under investigation. This is because the contributions from $\tilde{H}$ and $\tilde{E}$, the GPDs which are responsible for the leading-twist structure function σ_L, are very small compared with the contributions from $\bar{E}_T$ and H_T, which contribute to $d\sigma_T/dt$ and $d\sigma_{TT}/dt$. In addition, the transverse cross sections are strongly enhanced by the chiral condensate through the parameter $\mu_\pi = m_\pi^2/(m_u + m_d)$, where m_u and m_d are current quark masses [12].

With the inclusion of the quark-helicity nonconserving chiral-odd GPDs, which contribute primarily to $d\sigma_T/dt$ and $d\sigma_{TT}/dt$ and, to a lesser extent, to $d\sigma_{LT}/dt$, the model of Ref. [18] agrees rather well with the data. Deviations in shape

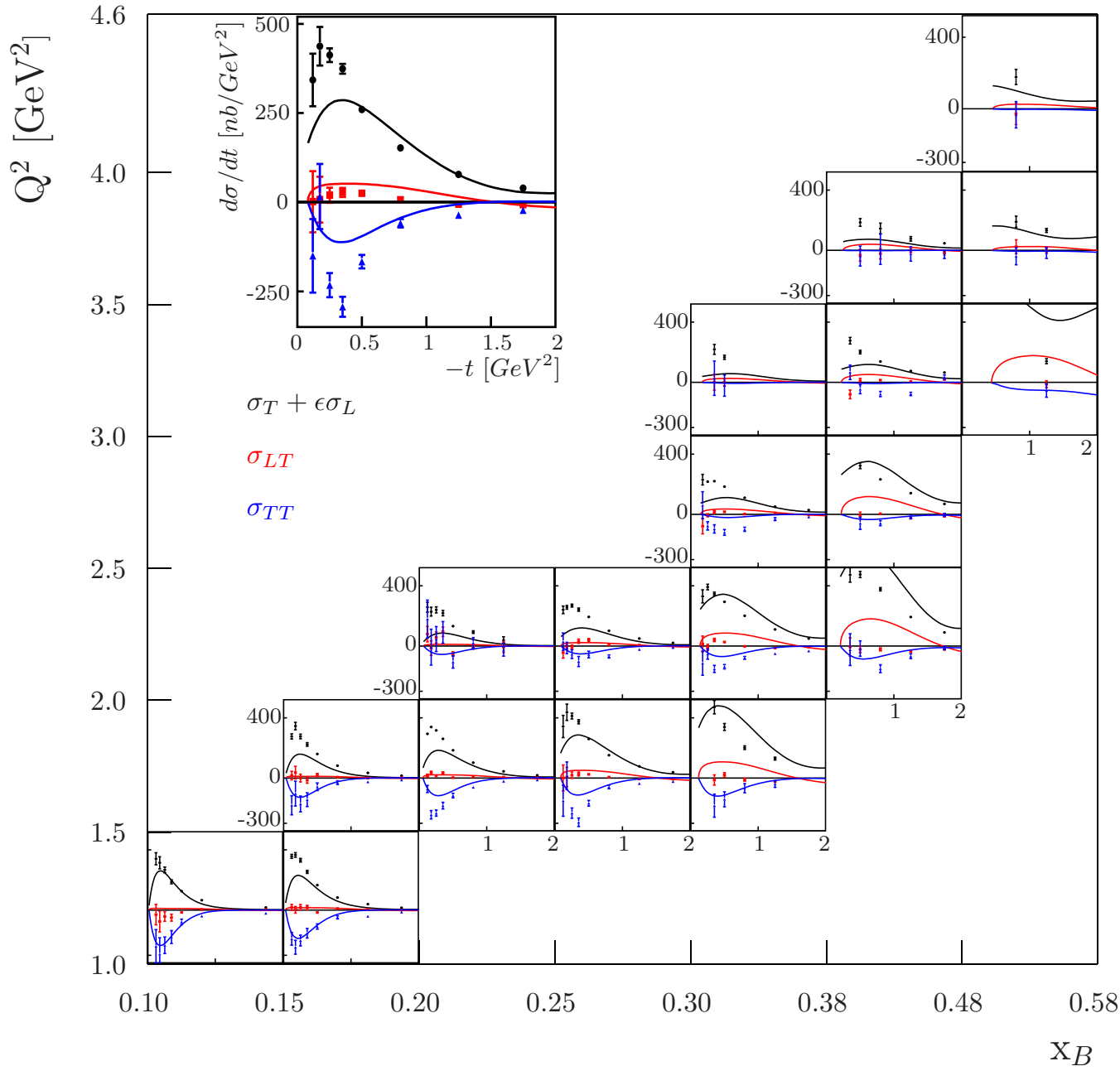

FIG. 20. (Color online) Structure functions $d\sigma_U/dt = d\sigma_T/dt + \epsilon d\sigma_L/dt$ (black circles), $d\sigma_{TT}/dt$ (blue triangles), and $d\sigma_{LT}/dt$ (red squares) as a function of $-t$ for different Q^2 and x_B for the reaction $\gamma^* p \to p'\pi^0$. All the structure functions are numerically given in Appendix C. The error bars are statistical only. The point-by-point propagated systematic uncertainties for all the structure functions are given in Appendix C. The curves are the results of a Regge-based calculation [20]: black (positive), $d\sigma_U/dt$; blue (negative), $d\sigma_{TT}/dt$; and red (small), $d\sigma_{LT}/dt$. Note that in the higher-x_B/lower-Q^2 bins the black curves ($d\sigma_U/dt$) from the model are much higher than the data and become off scale.

become greater at smaller $-t$ for the unseparated cross section $d\sigma_U/dt$. The behavior of the cross section as $|t| \to |t|_{\min}$ is determined by the interplay between H_T and $\bar{E}_T$. For the GPDs of Ref. [18] the parametrization was guided by the lattice calculation results of Ref. [34], while Ref. [19] used a GPD Reggeized diquark-quark model to obtain the GPDs. The results in Fig. 23 for the model of Ref. [18] (solid curves), in which $\bar{E}_T$ is dominant, agree rather well with the data. In particular, the structure function $d\sigma_U/dt$ begins to decrease as $|t| \to |t|_{\min}$, showing the effect of $\bar{E}_T$. In the model of Ref. [19] (dashed curves) H_T is dominant, which leads to a large rise in cross section as $-t$ becomes small so that the contribution of $\bar{E}_T$ relative to H_T appears to be underestimated. One can make a similar conclusion from the

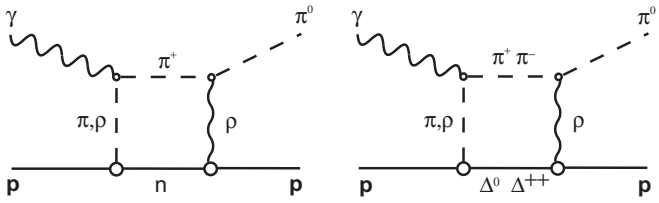

FIG. 21. Rescattering diagrams with the pion charge-exchange processes included in Ref. [20]. The vertical dashed and wavy lines represent the exchange of Regge trajectories. The horizontal lines correspond to on-shell meson nucleon rescattering processes.

comparison between data and model predictions for σ_{TT}. This shows the sensitivity of the measured π^0 structure functions for constraining the transversity GPDs. From Eq. (10) for $d\sigma_T/dt$ and Eq. (11) for $d\sigma_{TT}/dt$ one can conclude that $|d\sigma_{TT}/dt| < d\sigma_T/dt < d\sigma_U/dt$. One sees from Fig. 23 that $-d\sigma_{TT}/dt$ is a sizable fraction of the unseparated cross section, while $d\sigma_{LT}/dt$ is very small, which implies that contributions from transversity GPDs play a dominant role in the π^0 electroproduction process.

Figure 24 shows the extracted structure functions vs t for all kinematic bins, but this time compared to the GPD calculations of Ref. [18]. While $d\sigma_{LT}/dt$ is very small in all kinematic bins, $d\sigma_{TT}/dt$ remains substantial, which is what one would expect for a transverse photon dominated process.

XI. CONCLUSION

Differential cross sections of exclusive neutral-pion electroproduction have been obtained in the few-GeV region at more than 1800 kinematic points in bins of Q^2,x_B, t, and ϕ_π. Virtual-photon structure functions $d\sigma_U/dt$, $d\sigma_{TT}/dt$, and $d\sigma_{LT}/dt$ have been obtained. It is found that $d\sigma_U/dt$ and $d\sigma_{TT}/dt$ are comparable in magnitude with each other, while $d\sigma_{LT}/dt$ is very much smaller than either. The t-dependent distributions of the structure functions have been compared with calculations based upon the Regge trajectory and handbag approaches. In each case, it is found that the cross sections are dominated by transverse photons.

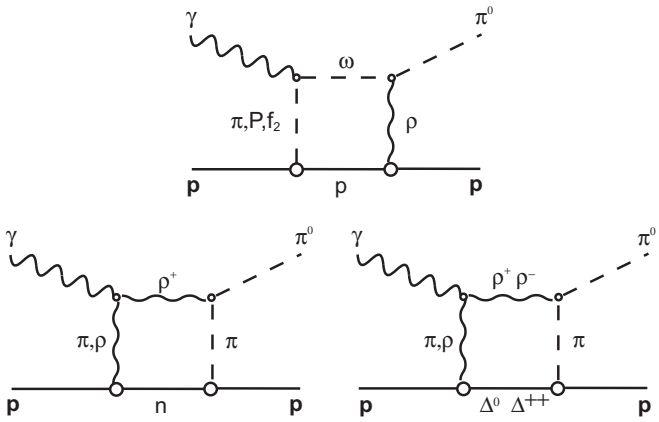

FIG. 22. Rescattering diagrams with vector meson processes included in Ref. [20].

In the Regge model [20], to account for the magnitude of the cross section, it has been necessary to add vector meson rescattering amplitudes (Fig. 22) to the original pole terms and pseudoscalar rescattering amplitudes (Fig. 21).

Within the handbag interpretation, there are two independent theoretical calculations [18,19]. They confirm that the measured unseparated cross sections are much larger than expected from leading-twist handbag calculations which are dominated by longitudinal photons. The same conclusion can be made in an almost model-independent way by noting that the structure functions $d\sigma_U/dt$ and $d\sigma_{TT}/dt$ are comparable to each other while $d\sigma_{LT}$ is quite small in comparison. In the calculation of Ref. [19] the dominant GPD is H_T, which involves a nucleon helicity flip, while that of Ref. [18] has a larger contribution of $\bar{E}_T$, which involves a nucleon nonhelicity flip. The data at t near $t_{\min}$ appear to favor the calculation of Ref. [18]. In Eqs. (B21)–(B23) one can make two observations. First, note that cross-section contributions owing to $\bar{E}_T$ vanish as $|t| \to |t|_{\min}$. There is no such constraint on terms involving H_T. The observed $d\sigma_U/dt$ does appear to turn over as $|t| \to |t|_{\min}$, which is expected when the contribution of $\bar{E}_T$ is relatively large, as in Ref. [18]. Second, the structure function $d\sigma_{TT}/dt$, which depends on $\bar{E}_T$, is relatively large in the data.

However, one must be very cautious not to overinterpret the results at this time. Detailed interpretations are model dependent and quite dynamic in that they are strongly influenced by new data as they become available. In particular, calculations are in progress to compare the theoretical models with the beam-spin asymmetries obtained earlier with CLAS [16] and longitudinal target spin asymmetries, also obtained with CLAS, which are currently under analysis [35].

Extracting $d\sigma_L/dt$ and $d\sigma_T/dt$ and performing new measurements with transversely and longitudinally polarized targets would also be very useful and are planned for the future Jefferson Lab at 12 GeV. In addition to nonpolarized cross sections, which are the subject of the present article, the measurement of beam and target spin asymmetries can provide further constraints on the theoretical handbag models considered here. Beam-spin asymmetry data at similar kinematic coverage were published by Ref. [16] and in a smaller kinematic range in Ref. [14]. Extensive new CLAS measurements of beam spin, target spin, and double-spin asymmetries are currently under analysis. Comparison of these results with the predictions of the handbag models is currently being studied.

ACKNOWLEDGMENTS

We thank the staff of the Accelerator and Physics Divisions at Jefferson Lab for making the experiment possible. We also thank G. Goldstein, S. Goloskokov, P. Kroll, J. M. Laget, and S. Liuti for many informative discussions and clarifications of their work and making available the results of their calculations. This work was supported in part by the US Department of Energy and National Science Foundation, the French Centre National de la Recherche Scientifique and Commissariat à l'Energie Atomique, the French-American Cultural Exchange (FACE), the Italian Istituto Nazionale di Fisica Nucleare,

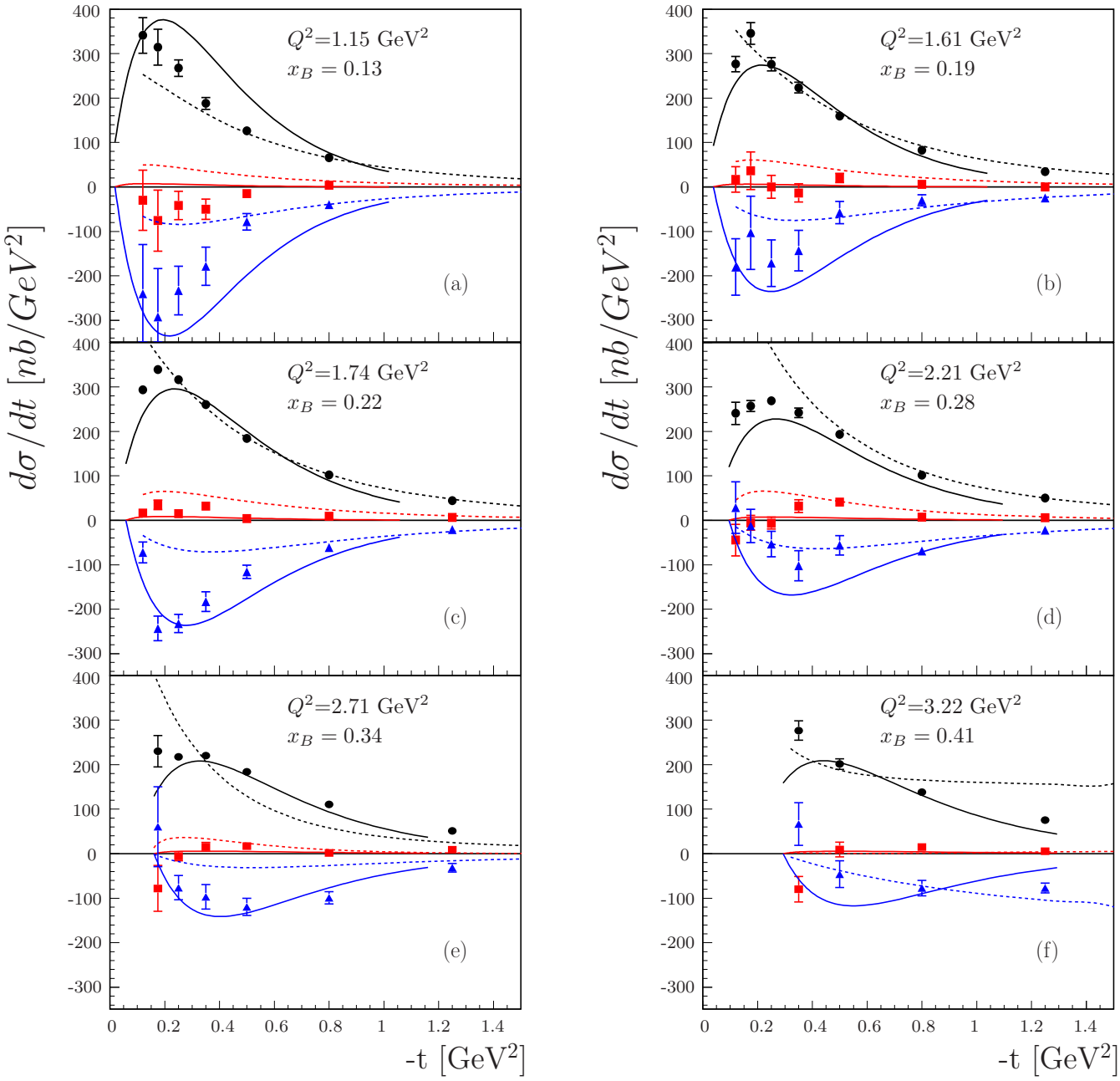

FIG. 23. (Color online) The extracted structure functions vs t for the bins with the best kinematic coverage and for which there are theoretical calculations. The data and curves are as follows: black (solid circles), $d\sigma_U/dt = d\sigma_T/dt + \epsilon d\sigma_L/dt$; blue (triangles), $d\sigma_{TT}/dt$; and red (squares), $d\sigma_{LT}/dt$. All the structure functions are numerically given in Appendix C. The error bars are statistical only. The point-by-point propagated systematic uncertainties for all the structure functions are given in Appendix C. The curves are theoretical predictions produced with the models of Refs. [18] (solid) and [19] (dashed). In particular, black (positive), $d\sigma_U/dt (= d\sigma_T/dt + \epsilon d\sigma_L/dt)$; blue (negative), $d\sigma_{TT}/dt$; and red (small), $d\sigma_{LT}/dt$.

the Chilean Comisión Nacional de Investigación Científica y Tecnológica (CONICYT), the National Research Foundation of Korea, and the UK Science and Technology Facilities Council (STFC). The Jefferson Science Associates (JSA) operates the Thomas Jefferson National Accelerator Facility for the United States Department of Energy under Contract No. DE-AC05-06OR23177.

APPENDIX A: KINEMATICS

The kinematic variables of the process

$$e(k) + p(p) \rightarrow e'(k') + p'(p') + \pi^0(v)$$

are defined as follows. The 4-momenta of the incident and outgoing electrons are denoted by k and k' and the 4-momentum

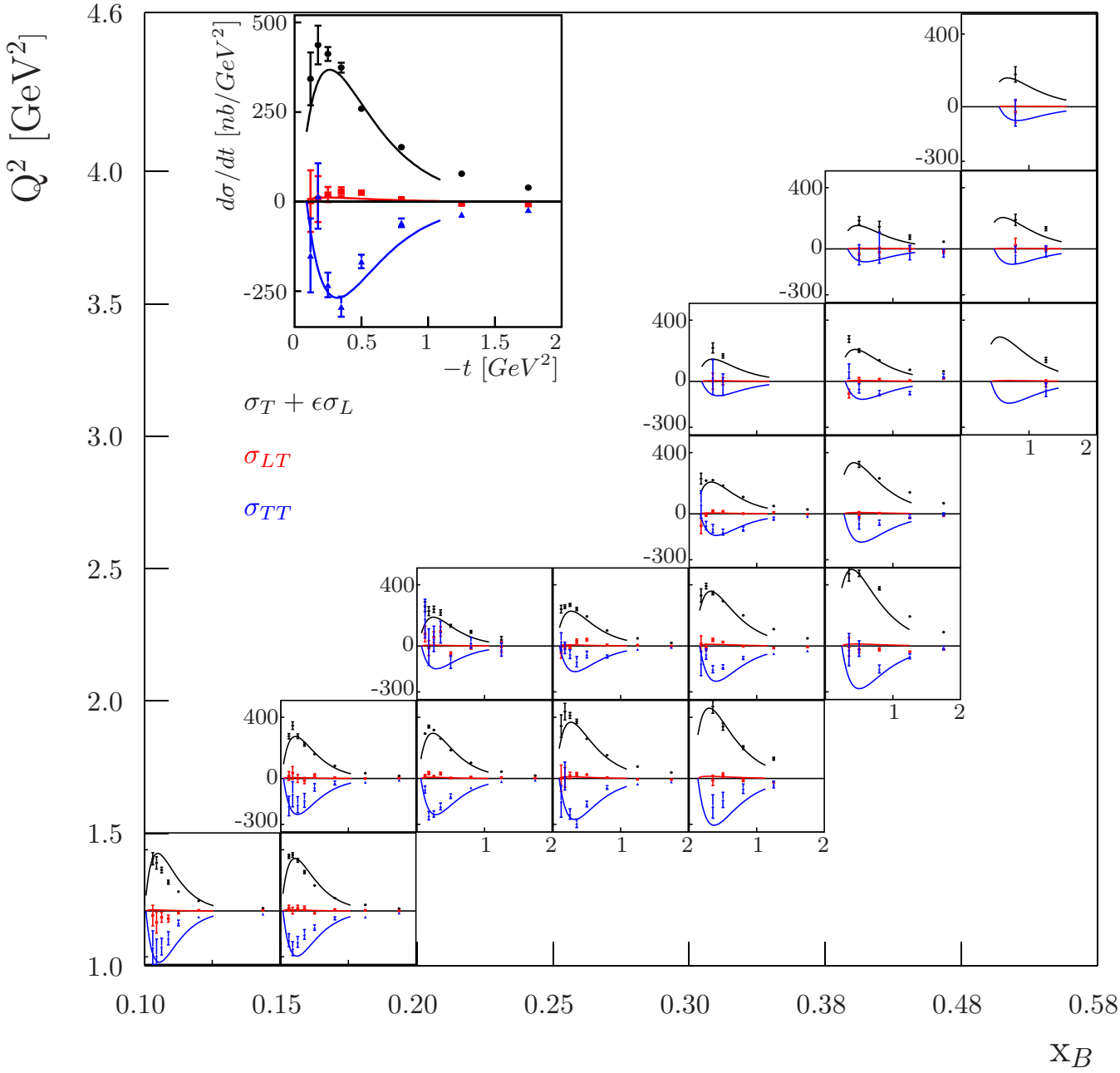

FIG. 24. (Color online) The extracted structure functions vs t as in Fig. 20 for all kinematic bins. The data and curves are as follows: black (positive) $d\sigma_U/dt = d\sigma_T/dt + \epsilon d\sigma_L/dt$, blue (negative) $d\sigma_{TT}/dt$, and red (small) $d\sigma_{LT}/dt$. All the structure functions are numerically given in Appendix C. The error bars are statistical only. The point-by-point propagated systematic uncertainties are given in the table in Appendix C. The curves are theoretical predictions for these structure functions obtained in the framework of the handbag model by Ref. [18]. As before, black (positive) $d\sigma_U/dt = d\sigma_T/dt + \epsilon d\sigma_L/dt$, blue (negative) $d\sigma_{TT}/dt$, and red (small)-$d\sigma_{LT}/dt$.

of the virtual photon q is defined as $q = k - k'$. In the laboratory system θ is the scattering angle between the incident and outgoing electrons, with energies E and E', respectively. The photon virtuality, given by

$$Q^2 = -q^2 = -(k - k')^2 \approx 4\, E\, E' \sin^2 \frac{\theta}{2}, \qquad \text{(A1)}$$

is positive. The 4-momenta of the incident and outgoing protons are denoted by p and p'. The energy of the virtual photon is

$$\nu = \frac{pq}{m} = E - E', \qquad \text{(A2)}$$

where m is the proton mass. The Bjorken scaling variable x_B is defined as

$$x_B = \frac{Q^2}{2pq} = \frac{Q^2}{2m\nu}. \qquad \text{(A3)}$$

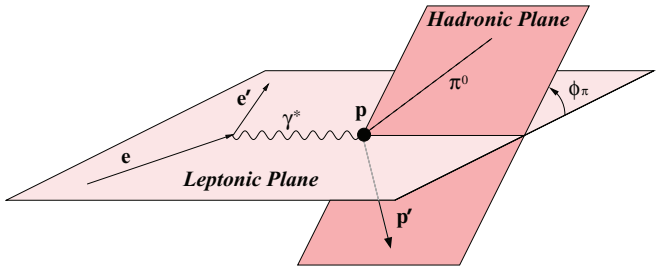

FIG. 25. (Color online) The kinematics of π^0 electroproduction. ϕ_π is the angle between the lepton and hadron planes. The lepton plane is defined by the incident and the scattered electron. The hadron plane is defined by the π^0 and the scattered proton.

The squared invariant mass of the photon-proton system is given by

$$W^2 = (p+q)^2 = m^2 + 2m\nu - Q^2. \tag{A4}$$

The momentum transfer t to the proton is defined by the relation

$$t = (p-p')^2 = (q-p_\pi)^2, \tag{A5}$$

where p_π is the 4-momentum of the π^0 meson. The minimum momentum transfer for a given Q^2 and W (or x_B) is denoted by $t_{\min}$.

The angle ϕ_π between the leptonic and hadronic planes is defined according to the Trento convention [36] (see Fig. 25).

APPENDIX B: HELICITY AMPLITUDES AND GENERALIZED PARTON DISTRIBUTIONS

Under the assumption of single-photon exchange, the differential cross section of the reaction $ep \to e'p'\pi^0$ for an unpolarized electron beam and proton target can be written as [12]

$$\frac{d^4\sigma}{dQ^2 dx_B dt d\phi_\pi} = \Gamma(Q^2,x_B,E)\frac{1}{2\pi}\left[\left(\frac{d\sigma_T}{dt}+\epsilon\frac{d\sigma_L}{dt}\right) + \epsilon\cos 2\phi_\pi\frac{d\sigma_{TT}}{dt} + \sqrt{2\epsilon(1+\epsilon)}\cos\phi_\pi\frac{d\sigma_{LT}}{dt}\right], \tag{B1}$$

where $\Gamma(Q^2,x_B,E)$ is the flux of transverse virtual photons and σ_T, σ_L, σ_{TT}, and σ_{LT} are the structure functions. They depend, in general, on the variables Q^2, x_B, and t. The Hand convention [27] was adopted for the definition of the virtual-photon flux factor $\Gamma(Q^2,x_B,E)$,

$$\Gamma(Q^2,x_B,E) = \frac{\alpha}{8\pi}\frac{Q^2}{m^2E^2}\frac{1-x_B}{x_B^3}\frac{1}{1-\epsilon}, \tag{B2}$$

and α is the standard electromagnetic coupling constant. The variable ϵ represents the ratio of fluxes of longitudinally and transversely polarized virtual photons and is given by

$$\epsilon = \frac{1-y-\frac{Q^2}{4E^2}}{1-y+\frac{y^2}{2}+\frac{Q^2}{4E^2}}, \tag{B3}$$

with $y = pq/qk = \nu/E$.

The reduced cross section is defined as

$$\frac{d^2\sigma}{dt d\phi_\pi} = \frac{1}{2\pi}\left[\left(\frac{d\sigma_T}{dt}+\epsilon\frac{d\sigma_L}{dt}\right) + \epsilon\cos 2\phi_\pi\frac{d\sigma_{TT}}{dt} + \sqrt{2\epsilon(1+\epsilon)}\cos\phi_\pi\frac{d\sigma_{LT}}{dt}\right]. \tag{B4}$$

Six independent helicity amplitudes $M_{\mu'\nu'\mu\nu}$ describe the π^0 electroproduction process $\gamma^* p \to \pi^0 p'$. With reference to Fig. 2, μ and μ' label the helicities of the virtual photon ($\mu = 0,+1,-1$) and π^0 ($\mu' = 0$). The helicities of protons before and after the interaction are labeled ν and ν', respectively. We denote "+" for the $\nu = 1/2$ and "−" for $\nu = -1/2$. The unmeasured helicities of the emitted and absorbed quarks are denoted λ and λ' as in Fig. 2. Four of these amplitudes describe the reaction initiated by transversely polarized photons: M_{0-++}, M_{0--+}, M_{0+++}, M_{0+-+}. The first two correspond to nucleon helicity flip and the latter two to nucleon helicity nonflip. There are two amplitudes which describe the reaction owing to longitudinally polarized photons (M_{0+0+}, M_{0-0+}), with nucleon helicity nonflip and helicity flip, respectively. It is convenient to introduce two new amplitudes with so-called natural $M^N_{0\nu'\mu\nu}$ and unnatural $M^U_{0\nu'\mu\nu}$ exchanges:

$$M^N_{0\nu'\mu\nu} = \tfrac{1}{2}[M_{0\nu'\mu\nu} + M_{0\nu'-\mu\nu}], \tag{B5}$$

$$M^U_{0\nu'\mu\nu} = \tfrac{1}{2}[M_{0\nu'\mu\nu} - M_{0\nu'-\mu\nu}]. \tag{B6}$$

The former does not change sign upon photon helicity reversal, and the latter changes sign upon photon helicity reversal.

The inverse equations are

$$M_{0\nu'\mu\nu} = M^N_{0\nu'\mu\nu} + M^U_{0\nu'\mu\nu}, \tag{B7}$$

$$M_{0\nu'-\mu\nu} = M^N_{0\nu'\mu\nu} - M^U_{0\nu'\mu\nu}. \tag{B8}$$

For $t' \to 0$ a helicity amplitude vanishes (at least) as $M_{\mu'\nu'\mu\nu} \propto \sqrt{-t'}^{|\mu-\nu-\mu'+\nu'|}$ as a consequence of angular momentum conservation, where $t' = t - t_{\min}$. Thus, for transverse photons, for nucleon helicity flip ($\nu' = -\nu$) the cross sections may remain finite at $t' \to 0$, while for nucleon helicity nonflip ($\nu' = \nu$), the cross section should approach 0 as $t' \to 0$. According to the findings in Refs. [12,18] and the HERMES measurement of the transverse-spin asymmetry A_{UT}, as well as the CLAS measurement of the π^0 cross section [13], it seems that the following hierarchy of the amplitudes for transversely polarized photons holds:

$$|M_{0--+}|, |M^U_{0+++}| \ll |M_{0-++}|, |M^N_{0+++}|. \tag{B9}$$

The structure functions can be written in terms of the helicity amplitudes, neglecting the smallest amplitudes: See Eq. (B9) above.

The longitudinal structure function σ_L is connected to longitudinally polarized photons:

$$\frac{d\sigma_L}{dt} = \frac{1}{k}[|M_{0+0+}|^2 + |M_{0-0+}|^2]. \tag{B10}$$

The structure function σ_T involves transversely polarized photons:

$$\begin{aligned}\frac{d\sigma_T}{dt} &= \frac{1}{2k}[|M_{0-++}|^2 + |M_{0--+}|^2 + |M_{0+++}|^2 + |M_{0+-+}|^2] \\ &\simeq \frac{1}{2k}[|M_{0-++}|^2 + 2\left|M^N_{0+++}\right|^2]. \end{aligned}\tag{B11}$$

The structure function σ_{LT} involves the interference between the longitudinal and transverse amplitudes,

$$\begin{aligned}\frac{d\sigma_{LT}}{dt} &= -\frac{1}{\sqrt{2}k}\mathrm{Re}[M^*_{0-0+}(M_{0-++} - M_{0--+}) \\ &\quad + 2M^*_{0+0+}M_{0+-+}] \\ &\simeq -\frac{1}{\sqrt{2}k}\mathrm{Re}(M^*_{0-++}M_{0-0+}). \end{aligned}\tag{B12}$$

Likewise, the transverse-transverse interference cross section σ_{TT} is

$$\begin{aligned}\frac{d\sigma_{TT}}{dt} &= -\frac{1}{k}\mathrm{Re}[M^*_{0-++}M_{0--+} + M^*_{0+++}M_{0+-+}] \\ &\simeq -\frac{1}{k}\left|M^N_{0+++}\right|^2. \end{aligned}\tag{B13}$$

The quantity k is the phase space factor, which depends on W^2, Q^2, m^2, and x_B, and varies approximately as Q^4:

$$\begin{aligned} k &= 16\pi(W^2 - m^2)\sqrt{\Lambda(W^2, -Q^2, m^2)} \\ &= 16\pi Q^2\left(\frac{1}{x_B} - 1\right) \\ &\quad \times \sqrt{(W^2 - m^2)^2 + Q^4 + 2W^2Q^2 + 2Q^2m^2} \\ &= Q^4k'. \end{aligned}\tag{B14}$$

In the GPD-handbag approximation, exclusive π^0 electroproduction can be decomposed into a hard part, describing the partonic subprocess and a soft part that contains the GPDs. This factorization occurs at large photon virtualities Q^2 and small momentum transfer to the nucleon, $-t$. Following the notation of Ref. [18], the connection between the helicity amplitudes and GPDs is

$$M_{0+0+} = \sqrt{1-\xi^2}\frac{e_0}{Q}\left[\langle\tilde{H}\rangle - \frac{\xi^2}{1-\xi^2}\langle\tilde{E}\rangle\right], \tag{B15}$$

$$M_{0-0+} = -\frac{e_0}{Q}\frac{\sqrt{-t'}}{2m}\xi\langle\tilde{E}\rangle, \tag{B16}$$

$$M_{0-++} = e_0\frac{\mu_\pi}{Q^2}\sqrt{1-\xi^2}\langle H_T\rangle, \tag{B17}$$

$$M^N_{0+++} = -e_0\frac{\mu_\pi}{Q^2}\frac{\sqrt{-t'}}{4m}\langle\bar{E}_T\rangle. \tag{B18}$$

The variable $\xi \simeq \frac{x_B(1+m_p^2/Q^2)}{(2-x_B)}$, $\mu_\pi = m_\pi^2/(m_u + m_d)$, where m_u and m_d are current quark masses [12], and $\bar{E}_T \equiv 2\widetilde{H}_T + E_T$. $\langle F\rangle$ denotes a convolution of GPD F with the hard-scattering kernel, $\mathcal{H}_{\mu'\lambda'\mu\lambda}$, where λ and λ' are the (unmeasured) helicities of the incoming and outgoing quarks, μ is the virtual-photon helicity, and $\mu = 0$ is the neutral-pion helicity, and is given by

$$\langle F\rangle \equiv \sum_\lambda \int_{-1}^{1} dx \mathcal{H}_{\mu'\lambda'\mu\lambda}F. \tag{B19}$$

$\langle H_T\rangle$ arises primarily from nucleon helicity-flip processes, while $\langle\bar{E}_T\rangle$ describes nucleon helicity nonflip processes.

Note that a factor $1/Q$ in the longitudinal amplitudes and a factor μ_π/Q^2 in the transverse amplitudes has been factored to explicitly show the leading Q^2 dependence. The convolutions $\langle F\rangle$ are still Q^2 dependent owing to evolution, the running of α_s, and other effects. In the convolutions there is also a summation over the parton helicities.

Combining the above finally yields the GPD dependence of the structure functions:

$$\frac{d\sigma_L}{dt} = \frac{4\pi\alpha}{k'}\frac{1}{Q^6}\left\{(1-\xi^2)|\langle\tilde{H}\rangle|^2 - 2\xi^2\mathrm{Re}[\langle\tilde{H}\rangle^*\langle\tilde{E}\rangle] - \frac{t'}{4m^2}\xi^2|\langle\tilde{E}\rangle|^2\right\}, \tag{B20}$$

$$\frac{d\sigma_T}{dt} = \frac{4\pi\alpha}{2k'}\frac{\mu_\pi^2}{Q^8}\left[(1-\xi^2)|\langle H_T\rangle|^2 - \frac{t'}{8m^2}|\langle\bar{E}_T\rangle|^2\right], \tag{B21}$$

$$\frac{d\sigma_{LT}}{dt} = \frac{4\pi\alpha}{\sqrt{2}k'}\frac{\mu_\pi}{Q^7}\xi\sqrt{1-\xi^2}\frac{\sqrt{-t'}}{2m}\mathrm{Re}[\langle H_T\rangle^*\langle\tilde{E}\rangle], \tag{B22}$$

$$\frac{d\sigma_{TT}}{dt} = \frac{4\pi\alpha}{k'}\frac{\mu_\pi^2}{Q^8}\frac{t'}{16m^2}|\langle\bar{E}_T\rangle|^2. \tag{B23}$$

APPENDIX C: STRUCTURE FUNCTIONS

The structure functions are presented in Table VIII.

TABLE VIII. Structure functions. The first error is statistical and the second is the systematic uncertainty.

Q^2 (GeV^2)	x_B	$-t$ (GeV^2)	$\frac{d\sigma_T}{dt} + \epsilon\frac{d\sigma_L}{dt}$ (nb/GeV^2)			$\frac{d\sigma_{LT}}{dt}$ (nb/GeV^2)			$\frac{d\sigma_{TT}}{dt}$ (nb/GeV^2)		
1.14	0.131	0.12	341	±40	±59	−30	±68	±114	−240	±111	±156
1.15	0.132	0.17	314	±40	±75	−76	±69	±126	−292	±108	±215
1.15	0.132	0.25	267	±19	±15	−42	±32	±37	−233	±55	±21
1.15	0.132	0.35	188	±13	±33	−50	±23	±43	−179	±43	±66
1.15	0.132	0.49	126.3	±4.7	±10	−15.0	±8.0	±5.5	−78	±19	±8.1
1.15	0.132	0.77	66.0	±2.0	±7.9	3.8	±3.1	±6.4	−39.8	±7.8	±16
1.16	0.133	1.71	17.8	±2.0	±1.6	4.3	±1.2	±2.0	−21.2	±6.6	±7.7
1.38	0.169	0.12	357	±13	±35	19	±19	±30	−191	±42	±47
1.38	0.169	0.17	366	±15	±24	2	±22	±21	−247	±46	±53
1.38	0.169	0.25	331	±12	±16	19	±18	±17	−202	±36	±49
1.38	0.169	0.35	254	±10	±13	17	±15	±24	−153	±32	±25
1.38	0.169	0.49	166.2	±5.1	±12	−15.4	±7.1	±12	−109	±18	±18
1.38	0.169	0.77	83.4	±3.3	±4.1	9.7	±4.4	±10	−48.5	±9.6	±5.4
1.38	0.169	1.21	39.6	±1.7	±3.8	4.0	±1.7	±1.9	−40.8	±4.5	±3.0
1.38	0.170	1.71	15.3	±1.4	±1.5	0.81	±0.80	±1.6	−13.6	±4.0	±5.1
1.61	0.186	0.12	276	±17	±46	17	±29	±58	−180	±64	±71
1.61	0.186	0.18	345	±25	±57	36	±42	±102	−103	±82	±87
1.61	0.187	0.25	276	±15	±7.0	0	±26	±21	−171	±52	±41
1.61	0.187	0.35	223	±12	±11	−14	±20	±11	−143	±46	±46
1.61	0.187	0.49	159.8	±6.3	±11	20	±10	±11	−58	±25	±19
1.61	0.187	0.78	82.4	±3.2	±7.1	5.6	±4.8	±19	−30	±12	±27
1.61	0.187	1.21	34.5	±2.3	±3.0	0.1	±3.3	±1.7	−24.9	±6.4	±6.6
1.61	0.187	1.71	16.0	±1.9	±1.6	2.3	±1.8	±2.2	−12.2	±6.2	±4.6
1.74	0.223	0.25	316.7	±6.7	±9.2	14.9	±8.5	±19	−232	±20	±44
1.75	0.223	0.12	293.3	±7.8	±24	16.2	±9.8	±12	−72	±23	±13
1.75	0.223	0.17	339.3	±8.9	±26	35	±11	±8.3	−243	±28	±26
1.75	0.224	0.35	260.5	±7.0	±13	32.1	±9.2	±5.0	−183	±22	±20
1.75	0.224	0.49	184.4	±5.0	±8.6	3.6	±6.3	±3.7	−116	±15	±20
1.75	0.224	0.78	102.2	±2.4	±5.4	9.2	±3.1	±5.0	−61.0	±7.3	±12
1.75	0.224	1.22	44.5	±1.4	±3.0	6.3	±1.3	±2.2	−21.2	±4.1	±6.0
1.75	0.224	1.72	19.00	±1.00	±4.4	2.24	±0.85	±3.2	−12.3	±3.0	±5.4
1.87	0.270	0.12	342	±74	±108	1	±86	±72	−150	±103	±101
1.87	0.271	0.18	437	±54	±90	7	±64	±74	16	±91	±167
1.87	0.271	0.25	412	±19	±32	20	±21	±20	−233	±34	±39
1.87	0.271	0.35	374	±14	±26	27	±13	±20	−293	±28	±41
1.87	0.271	0.49	259.5	±7.3	±13	25.1	±7.2	±6.1	−167	±19	±14
1.87	0.271	0.78	151.8	±4.1	±7.8	6.4	±4.2	±5.7	−59	±12	±4.6
1.87	0.271	1.22	77.7	±3.0	±5.5	−5.7	±2.3	±2.8	−36.4	±7.4	±5.6
1.87	0.272	1.72	39.2	±2.1	±3.5	−7.0	±1.9	±1.9	−22.9	±4.6	±3.8
1.95	0.313	0.35	470	±44	±82	−13	±34	±18	−183	±77	±58
1.95	0.313	0.49	339	±23	±21	21	±15	±34	−140	±50	±43
1.95	0.313	0.78	202	±12	±13	−11.1	±9.4	±5.8	−67	±31	±23
1.96	0.313	1.22	129.4	±9.6	±17	−24.8	±8.3	±6.7	−39	±22	±21
2.10	0.238	0.12	258	±33	±81	79	±51	±109	179	±126	±218
2.10	0.238	0.35	219	±18	±8.1	95	±31	±10	91	±72	±46
2.10	0.238	0.49	132.5	±8.9	±13	−53	±15	±9.0	−105	±41	±28
2.10	0.238	0.78	92.6	±8.9	±9.2	−8	±13	±12	21	±35	±32
2.10	0.238	1.21	40	±21	±16	−6	±35	±31	−23	±43	±27
2.10	0.239	0.17	228	±29	±148	−13	±49	±265	−7	±119	±268

TABLE VIII. *(Continued.)*

Q^2 (GeV^2)	x_B	$-t$ (GeV^2)	$\frac{d\sigma_T}{dt} + \epsilon\frac{d\sigma_L}{dt}$ (nb/GeV^2)			$\frac{d\sigma_{LT}}{dt}$ (nb/GeV^2)			$\frac{d\sigma_{TT}}{dt}$ (nb/GeV^2)		
2.10	0.239	0.25	240	±20	±24	57	±36	±30	47	±83	±106
2.21	0.275	0.12	241	±25	±11	−44	±36	±9.0	29	±58	±17
2.21	0.276	0.17	257	±12	±18	−6	±17	±13	−13	±38	±41
2.21	0.276	0.25	268.8	±9.8	±19	−6	±13	±20	−54	±29	±30
2.21	0.276	0.35	242	±11	±11	32	±14	±12	−102	±34	±22
2.21	0.276	0.49	193.5	±7.1	±17	41.1	±9.4	±20	−56	±22	±47
2.21	0.276	0.78	101.4	±3.0	±6.6	7.3	±4.3	±7.0	−69	±10	±10
2.21	0.277	1.22	50.0	±2.0	±3.3	5.8	±2.3	±3.9	−22.5	±6.9	±2.4
2.21	0.277	1.72	20.8	±1.5	±3.1	−0.1	±1.8	±2.3	−10.1	±4.8	±5.3
2.24	0.332	0.18	330	±44	±31	14	±53	±37	−114	±80	±118
2.24	0.337	0.25	392	±19	±44	−8	±20	±34	−53	±34	±27
2.24	0.338	0.49	293.7	±6.5	±15	26.4	±5.5	±13	−137	±14	±12
2.25	0.337	0.35	346	±12	±14	40	±11	±12	−152	±24	±15
2.25	0.338	0.78	200.8	±3.8	±13	−2.1	±3.3	±5.0	−78.6	±9.7	±10
2.25	0.339	1.22	110.2	±2.6	±5.4	−13.3	±2.3	±4.2	−50.4	±6.5	±6.1
2.25	0.339	1.73	49.9	±1.7	±4.6	−6.5	±1.8	±5.7	−32.3	±3.7	±5.8
2.34	0.403	0.35	472	±48	±53	−6	±60	±79	−24	±105	±210
2.34	0.403	0.49	475	±20	±39	−22	±23	±27	−17	±51	±53
2.34	0.404	0.78	377	±11	±17	−22	±10	±5.8	−150	±26	±19
2.34	0.404	1.22	192.8	±7.4	±13	−37.3	±7.9	±4.4	−67	±16	±43
2.35	0.404	1.73	90.5	±6.6	±3.1	−22.4	±7.4	±5.7	−13	±12	±8.4
2.71	0.336	0.18	230	±35	±29	−78	±52	±84	60	±90	±188
2.71	0.343	0.25	217.3	±8.1	±10	−6	±10	±4.3	−76	±27	±22
2.71	0.343	0.35	220.5	±8.1	±8.0	15.5	±9.8	±7.6	−97	±27	±28
2.71	0.343	0.49	183.8	±6.0	±9.4	17.0	±7.4	±12	−120	±19	±31
2.71	0.343	1.22	51.3	±2.4	±4.5	9.0	±2.7	±5.0	−31.5	±9.7	±16
2.72	0.344	0.78	110.4	±3.6	±5.8	1.8	±4.7	±5.8	−99	±14	±20
2.72	0.344	1.73	28.7	±1.9	±3.5	−2.9	±2.2	±2.0	−17.2	±5.6	±9.2
2.75	0.423	0.50	323	±19	±21	−8	±23	±16	−60	±40	±16
2.75	0.423	0.78	232.4	±6.9	±17	4.3	±6.4	±16	−58	±17	±24
2.75	0.424	1.23	140.7	±4.9	±9.0	−25.8	±5.6	±5.8	−16	±13	±12
2.75	0.424	1.73	69.3	±4.6	±2.9	−12.8	±5.3	±3.7	−2.7	±9.6	±12
3.12	0.362	0.35	219	±33	±139	1	±53	±213	27	±114	±398
3.12	0.362	0.50	167	±14	±20	1	±23	±59	−21	±71	±56
3.22	0.431	0.78	138.4	±6.2	±6.5	15.0	±7.9	±5.5	−77	±17	±16
3.23	0.428	0.35	277	±22	±15	−80	±29	±16	67	±48	±20
3.23	0.430	0.50	201	±12	±17	10	±16	±17	−46	±30	±31
3.23	0.432	1.23	75.5	±3.8	±9.2	5.6	±4.3	±12	−77	±11	±32
3.23	0.432	1.73	65.4	±5.0	±6.7	18.8	±5.7	±6.2	35	±14	±15
3.29	0.496	1.23	140	±17	±18	−12	±23	±9.7	−54	±45	±12
3.67	0.451	0.78	145	±36	±23	−22	±35	±28	8	±101	±56
3.67	0.451	1.23	77	±15	±1.8	2	±17	±2.9	−24	±48	±8.8
3.68	0.451	0.49	185	±26	±18	−32	±39	±29	−38	±66	±57
3.68	0.451	1.73	47.0	±6.9	±3.9	−14.7	±9.4	±7.3	−27	±27	±7.9
3.76	0.513	0.78	190	±37	±40	24	±46	±37	−39	±56	±41
3.76	0.514	1.23	132	±13	±11	1	±14	±8.4	−17	±37	±40
4.23	0.539	0.78	178	±42	±45	−28	±60	±57	−34	±74	±64

[1] X. Ji, Phys. Rev. Lett. **78**, 610 (1997); Phys. Rev. D **55**, 7114 (1997).

[2] A. V. Radyushkin, Phys. Lett. B **380**, 417 (1996); Phys. Rev. D **56**, 5524 (1997).

[3] J. C. Collins and A. Freund, Phys. Rev. D **59**, 074009 (1999).

[4] J. C. Collins, L. Frankfurt, and M. Strikman, Phys. Rev. D **56**, 2982 (1997).

[5] D. Mueller, D. Robaschik, B. Geyer, F. M. Dittes, and J. D. Horejsi, Fortsch. Phys. **42**, 101 (1994).

[6] C. M. Camacho *et al.* (HALL-A Collaboration), Phys. Rev. Lett. **97**, 262002 (2006).

[7] P. Hoodbhoy and X. Ji, Phys. Rev. D **58**, 054006 (1998).

[8] M. Diehl, Phys. Rep. **388**, 41 (2003), and references within.

[9] K. Goeke, M. V. Polyakov, and M. Vanderhaeghen, Prog. Part. Nucl. Phys. **47**, 401 (2001).

[10] M. I. Eides, L. I. Frankfurt, and M. I. Strikman, Phys. Rev. D **59**, 114025 (1999).

[11] H. W. Huang and P. Kroll, Eur. Phys. J. C **17**, 423 (2000).

[12] S. V. Goloskokov and P. Kroll, Eur. Phys. J. C **65**, 137 (2010).

[13] I. Bedlinskiy *et al.* (CLAS Collaboration), Phys. Rev. Lett. **109**, 112001 (2012).

[14] E. Fuchey *et al.* (HALL-A Collaboration), Phys. Rev. C **83**, 025201 (2011).

[15] A. Airapetian *et al.* (HERMES Collaboration), Phys. Lett. B **682**, 345 (2010).

[16] R. De Masi *et al.* (CLAS Collaboration), Phys. Rev. C **77**, 042201 (2008).

[17] S. Ahmad, G. R. Goldstein, and S. Liuti, Phys. Rev. D **79**, 054014 (2009).

[18] S. V. Goloskokov and P. Kroll, Eur. Phys. J. A **47**, 112 (2011).

[19] G. R. Goldstein, J. O. Hernandez, and S. Liuti, Phys. Rev. D **84**, 034007 (2011); G. Goldstein, J. O. Gonzalez-Hernandez, and S. Liuti, Int. J. Mod. Phys. Conf. Ser. **20**, 222 (2012); G. Goldstein, J. O. Gonzalez-Hernandez, and S. Liuti, J. Phys. G: Nucl. Part. Phys. **39**, 115001 (2012).

[20] J.-M. Laget, Phys. Lett. B **695**, 199 (2011), and references within.

[21] B. A. Mecking *et al.*, Nucl. Instrum. Methods Phys. Res., Sect. A **503**, 513 (2003).

[22] M. D. Mestayer *et al.*, Nucl. Instrum. Methods Phys. Res., Sect. A **449**, 81 (2000).

[23] G. S. Adams *et al.*, Nucl. Instrum. Methods Phys. Res., Sect. A **465**, 414 (2001).

[24] E. S. Smith *et al.*, Nucl. Instrum. Methods Phys. Res., Sect. A **432**, 265 (1999).

[25] M. Amarian *et al.*, Nucl. Instrum. Methods Phys. Res., Sect. A **460**, 239 (2001).

[26] A. Afanasev, I. Akushevich, V. Burkert, and K. Joo, Phys. Rev. D **66**, 074004 (2002).

[27] L. Hand, Phys. Rev. **129**, 1834 (1963).

[28] See Supplemental Material at http://link.aps.org/supplemental/10.1103/PhysRevC.90.025205 for differential cross sections for exclusive π^0 electroproduction $\frac{d^2\sigma}{dtd\phi_\pi}(\gamma^* p \to \pi^0 p)$.

[29] S. A. Morrow *et al.* (CLAS Collaboration), Eur. Phys. J. A **39**, 5 (2009).

[30] M. Burkardt, arXiv:0711.1881.

[31] J. M. Laget, Phys. Rev. C **73**, 044003 (2006).

[32] J. M. Laget, Phys. Lett. B **685**, 146 (2010).

[33] M. Diehl and Ph. Haegler, Eur. Phys. J. C **44**, 87 (2005).

[34] M. Gockeler *et al.* (QCDSF Collaboration and UKQCD Collaboration), Phys. Rev. Lett. **98**, 222001 (2007).

[35] A. Kim *et al.* (CLAS Collaboration) (unpublished).

[36] A. Bacchetta, U. D'Alesio, M. Diehl, and C. A. Miller, Phys. Rev. D **70**, 117504 (2004).